Preparation of sputter-deposited Cu-doped $BiVO_4$ nanoporous thin films comprised of amorphous/crystalline heterostructure as enhanced visible-light photocatalyst

Siavash Bakhtiarnia [a,b], Saeed Sheibani [a,*], Abbas Nadi [a], Eric Aubry [b, c], Hui Sun [d], Pascal Briois [b], Mohammad Arab Pour Yazdi [b, f]

[a] School of Metallurgy and Materials Engineering, College of Engineering, University of Tehran, Tehran, Iran.

[b] Institut FEMTO-ST, UMR 6174, CNRS, Université de Bourgogne Franche-Comté, UTBM, rue Ernest Thierry Mieg, Site de Montbéliard, 90010 Belfort cedex, France

[c] Institut FEMTO-ST, UMR 6174 CNRS, Université de Bourgogne Franche-Comté, UFC, 2 Place Lucien Tharradin, Site de Montbéliard, 25200 Montbéliard, France

[d] School of Space Science and Physics, Shandong University, Weihai 264209, China.

[f] Anton Paar TriTec SA, Les Vernets 6, 2035 Corcelles, Switzerland, https://www.anton-paar.com

*Corresponding author at School of Metallurgy and Materials Engineering, College of Engineering, University of Tehran, P.O. Box 11155-4563, Tehran, Iran. Tel.: +98 21 61114068; Fax: +98 21 88006076.

E-mail address: ssheibani@ut.ac.ir (S. Sheibani).

Abstract

The synthesis of Cu-doped $BiVO_4$ nanoporous thin films with various Cu contents was performed using reactive magnetron sputtering to prepare a stable and inexpensive photocatalyst

with high photoactivity under visible light for wastewater treatment applications. The X-ray diffraction (XRD) analysis showed exclusively the formation of the photoactive monoclinic $BiVO_4$ phase up to 17 at.% Cu. Beyond, a Cu-based compound crystallizes in addition to the $BiVO_4$ monoclinic phase. The field-emission scanning electron microscopy (FESEM) and elemental mappings results revealed the formation of shard-like nodules composed of V, O and Cu in the films having less than 6 at. % Cu. From 6 at. % Cu, the morphology appears more homogeneous. X-ray photoelectron spectroscopy (XPS) showed the presence of Cu^{2+} and Cu^{+}, as well as the rise of V^{4+}/V^{5+} ions. Transmission electron microscopy (TEM) verified the amorphous structure of the Cu-O-V phase, as well as demonstrated the crystallographic interplanar spacings of $BiVO_4$. The thin film with a 2 at. % Cu exhibited superior photoactivity (100, 99 and 63 %) over pristine $BiVO_4$ in photocatalytic dye degradation (Rhodamine-B, Methylene Blue and Methyl Orange). The thin films' stability, recyclability and reusability were demonstrated in the recycling experiment, and the crucial role of photogenerated charge carriers and hydroxyl radicals was identified in the experiment involving scavengers. The photocatalytic performance towards various dye pollutions at acidic, basic and neutral pH conditions is also discussed in detail.

Keywords: Photocatalyst; $BiVO_4$; Cu doping; Thin film; Sputtering; Nanoporous.

1. Introduction

Water scarcity is a serious concern heavily affecting the world. Preserving precious water resources is of great importance. In recent years, photocatalysis as a sustainable solution has been proposed for wastewater treatment applications employing semiconductors with high photoactivity under solar light as an unlimited source of energy [1]. A variety of semiconductor categories were employed and studied as photocatalysts such as nonmetallics (e.g. g-C_3N_4 and black phosphorous), metal calcogenides (e.g. CdS and CdTe), metal oxides (e.g. TiO_2, WO_3 and Cu_2O), metal-organic and covalent organic frameworks known as MOFs and COFs, transition metal carbides and nitrides (e.g. $Ti_3C_2T_x$), and bismuth-based materials (e.g. $BiVO_4$ and Bi_2WO_6) [2,3]. TiO_2 is the most adopted semiconductor in the field [4–6], though many drawbacks, including the lack of photoactivity under visible light on account of its wide bandgap (~3.2 eV) [7], lead the researchers to try developing alternative photocatalysts capable of harnessing a wider range of the solar spectrum [8]. $BiVO_4$ with a ~2.4 eV bandgap concerning the monoclinic scheelite crystal structure, received lots of attention as a visible-light-active semiconductor, along with advantages such as cost-efficiency, stability, high photoactivity under visible light and versatility in forming various morphology [9,10].

While $BiVO_4$ thin films have gained much interest as photoanodes for water-splitting applications [11,12], researchers showed a preference for the nanopowder form in photocatalysis due to some advantages namely facile synthesis, high specific surface and morphology control [13,14], but their nanometric size is problematic for their recyclability and reusability in industrial wastewater treatment [15,16]. Therefore, $BiVO_4$ thin-film photocatalysts enhanced with

nanoporous morphology could be a great candidate to substitute nanopowder photocatalysts raising the cost efficiency of photocatalytic water treatment [17].

Despite the advantages, $BiVO_4$ suffers some flaws including charge carrier mobility, recombination and low specific surface [18–20]. Certain solutions have been proposed to enhance the photoactivity of semiconductors. Our team has implemented Ag incorporation into pristine $BiVO_4$ thin films in previous research [21], and the results were promising with a 99 % visible-light photodegradation of RhB at neutral pH thanks to the charge separation of photogenerated electrons and holes due to $BiVO_4/Ag_4V_2O_7$ heterostructure, as well as the plasmonic effect of Ag nanoparticles improving the light absorption. In another research [22], $BiVO_4/Cu_2O$ nanocomposite with the p-n junction structure was prepared by mechanochemical synthesis, and the photocatalytic results showed 97 % MB photodegradation. The heterojunction between $BiVO_4$ (n-type) and Cu_2O (p-type) was proposed to be responsible for effective charge separation and reduction of recombination rate, as well as bandgap optimization (2.18 eV). Other solutions have also been explored, e.g., heterojunctions including p-n junction [23] and z-scheme [24], plasmonic sensitization [25], facet engineering [26] and the incorporation of transition metals [27]. Cu incorporation is considered to be a suitable candidate thanks to being inexpensive compared to noble metals, nontoxicity, antimicrobial properties and acting as electron traps [22,28,29]. The synthesis of $BiVO_4$ and metal incorporation both in powder or thin-film forms have been implemented by many methods such as hydrothermal [30], electrodeposition [31], sol-gel [32] and high energy ball milling [22], though vapor phase techniques did not receive proper attention. Few researchers selected the sputtering method to produce $BiVO_4$ thin films, and despite advantages

like uniform products, versatility, scalable and affordable production [33], publications on Cu-incorporated $BiVO_4$ using the sputtering technique are scarce in the literature [9,34].

This research aims to implement Cu incorporation into nanoporous $BiVO_4$ thin films employing reactive magnetron sputtering in a single step, which is unprecedented to the best of our knowledge. Further, to conduct a comparative analysis of the Cu content effect on the structural, microstructural and optical properties of the thin films through various characterization methods, as well as to investigate photocatalytic activity towards various dye pollutions at acidic, basic and neutral pH conditions. The mechanism of photodegradation using scavengers as the trapping agents of reactive species could help to have a deeper understanding of the Cu-incorporated thin films' photocatalytic function, and the recyclability experiment could ensure the suitable stability of the thin films which is critical for industrial applications. The results of this research contribute to making industrial photocatalytic wastewater treatment more practical and efficient, thus preserving the precious and scarce water resources more effectively.

2. Experimental procedure

2.1. Thin film deposition

Reactive magnetron sputtering as an environment-friendly technique was employed to synthesize the Cu-incorporated $BiVO_4$ thin films. Metallic cylindrical targets of Bi, V and Cu (50 $\times$ 3 mm^2) were utilized with a purity of 99.9 at. %. A turbomolecular pump provided the necessary vacuum below 10^{-4} Pa in the sputtering reactor (90 L cylinder, Alcatel) which utilizes four water-cooled magnetron sputtering sources. The Ar and O_2 gas flow rates were controlled and measured using flowmeters (Brooks). The working pressure of the device was measured with a Baratron

gauge (MKS). The discharge power was provided with a pulsed DC dual generator (Advanced Energy Pinnacle+) for Bi and V sources and a DC generator for Cu (Advanced Energy MDX 500). Adjusting the discharge power applied on each target allows to control of the chemical composition of the films (see Fig. S1 of the supplementary file). The films were deposited at room temperature on single crystal Si and fused silica ($76 \times 26 \times 1$ mm^3) substrates, which were cleaned before deposition and attached to a rotating holder kept parallel to the cathodes at a 60 mm distance to preserve any microstructural lateral gradient [35]. The thickness of the films was around 1 µm. The films underwent a post-annealing treatment at 450 ℃for 2 h in the air atmosphere to crystallize the samples. The deposition parameters are provided in **Table. 1**.

Table 1. The sputtering parameters for the deposition of thin films.

Ar flow rate (sccm)	200	**Targets**	Bi	V	Cu
O_2 flow rate (sccm)	20	**Intensity (A)**	0.08	0.67	0.004 → 0.016
Total pressure (Pa)	4.5	**Power (W)**	10	255	1 → 5
Runtime (min)	205	**Frequency (kHz)**	70	50	-
Drawing distance (mm)	60	**T_{off} (µs)**	4	4	-

2.2. Characterization methods

XRD using a cobalt X-ray tube (Co $_{K\alpha1+\alpha2}$ radiations $\lambda_{\alpha1}$ = 0.178897 nm and $\lambda_{\alpha2}$ = 0.179278 nm) was performed for crystallographic analysis (Bruker). The film's thickness was measured by a step method with an Altysurf Profilometer (Altisurf 500) manufactured by Altimet society. Before each measurement, the calibration of the device was performed with a reference sample number 787569 accredited by the CETIM organization. Ultraviolet-visible-near infrared (UV-Vis-

NIR) spectrophotometer (UV-3600, Shimadzu) equipped with an integration sphere (ISR-3100) was used for measuring the total reflectance and transmittance spectra of the thin films (220-2600 nm). A standard $BaSO_4$ reference was used for the baseline. The absorbance spectra were then calculated based on **Eq. 1** [36]. Using the absorbance and **Eq. 2** [36] the Tauc plots were illustrated to evaluate the bandgaps of the samples.

$$\alpha(\lambda) = \frac{1}{t} \ln\left(\frac{1 - R(\lambda)}{T(\lambda)}\right) \quad \textbf{(Eq. 1)}$$

$$(\alpha h\nu)^{1/n} = A\left(h\nu - E_g\right) \quad \textbf{(Eq. 2)}$$

Where $\alpha(\lambda)$ (cm^{-1}), $T(\lambda)$ (%) and $R(\lambda)$ (%) are absorption, transmission and reflection, respectively, as a function of wavelength. t, A, h and ν represent the film thickness (cm), a constant, Planck constant and photon frequency, respectively. E_g is the bandgap energy of the semiconductor and n depends on the direct (n = 0.5) or indirect (n = 2) nature of the bandgap. The direct bandgap nature of the $BiVO_4$ semiconductor was reported in the literature [37].

The microscopic top surface and brittle-fracture cross-section observation of the carbon-coated samples were implemented with FESEM (JEOL JSM-7800F). The chemical composition of the thin films was measured by Energy-Dispersive X-ray Spectroscopy (EDS, Bruker). Since the EDS method does not provide accuracy for oxygen, only the metallic elements were measured and the Cu contents reported in this work are the at. % ratio of Cu over Bi + V + Cu. TEM observations were also performed by JEOL JEM-2100 200 kV with 0.19 nm resolution equipped with EDS. Focused Ion Beam (FIB, Hitachi NX2000) was also employed in sample preparation stage. The interplanar spacings were calculated by the Fast Fourier Transform (FFT) method using

high-resolution TEM (HR-TEM) images. Selected area electron diffraction (SAED) patterns were also provided to further analyze the crystallographic structure.

The chemical oxidation state of the elements on the surface was analyzed by X-ray photoelectron spectroscopy (XPS) using ESCALAB 250 Xi (Thermo Fisher) equipped with monochromatic Al Kα X-rays. The Shirley background was adjusted for the spectra and the Lorentzian – Gaussian function was employed as the spectral shape line in peak deconvolutions. Valence band XPS (VB-XPS) was also employed to measure the valence band edge potential of the semiconductors. C 1s spectra of the samples were used for charge correction against the standard value of 284.8 eV and the carbon fermi level (0.3 V vs RHE) [38] is used as a reference for calculating band edge potentials. The photoluminescence (PL) spectra were measured using Varian Cary Eclipse Fluorescence Spectrophotometer with an excitation wavelength of 270 nm.

2.3. Photocatalytic experiment

Photocatalytic activity of the Cu-incorporated thin films was assessed under visible light (Metal halide 400 W, $\lambda > 400$ nm) using RhB, MB and MO dye solutions (5 mg/L) as sources of organic pollutions at various pH (3, 7 and 10) in a water-cooled homemade setup. Hydrochloric acid and ammonia were used to adjust the pH, and the samples were fixed at a 15 cm distance from the light source. The thin films were immersed in the dye solution (photocatalyst surface over dye solution volume: 0.1 cm^2/mL) 45 min before the illumination to ensure an adsorption-desorption equilibrium. Once the photocatalyst film was illuminated, 2 mL of the solution was collected every hour to measure the dye solution absorption using a UV-Vis spectrophotometer at the maximum wavelength of 464, 554 and 664 nm corresponding to MO, RhB and MB, respectively. The concentration was then calculated based on the Beer-Lambert law. The recycling experiment was

implemented for evaluating the stability of the films in 3 × 7 h consecutive cycles. To identify the reactive species involved in the photocatalytic mechanism, ethylenediaminetetraacetic acid disodium salt (EDTA, 10 mM), p-benzoquinone (p-BQ, 2 mM), cupric nitrate (CN, 10 mM) and methanol (10 mM) were used as the trapping agents of the photogenerated hole (h^+), superoxide ($^{\bullet}O_2^-$), electron (e^-) and hydroxyl radicals ($^{\bullet}OH$), respectively. The kinetics of the photocatalytic processes involving low concentrations of organic dyes is well accepted to be correspondent with the pseudo-first-order model following **Eq. 3** [39].

$$\ln\frac{C_0}{C} = k't \qquad \textbf{(Eq. 3)}$$

Where t is time (min), C_0 and C correspond to the initial concentration (g/L) and the concentration at t, respectively, as k′ represents the rate constant (min^{-1}).

3. Results and discussion

3.1. Structural and microstructural properties

According to the relatively high working pressure used in this study, the as-deposited thin films were amorphous, and therefore a post-annealing treatment for 2 h at 450 ℃under air was necessary to crystallize the photoactive monoclinic $BiVO_4$ structure. The XRD pattern of the pristine sample provided in **Fig. 1**, is well-matched with the monoclinic $BiVO_4$ crystal structure (m-$BiVO_4$, JCPDS No. 14-0688, space group: I2/a). Despite Cu incorporation to $BiVO_4$ thin films, no crystallized Cu-based compounds were detected up to 17 at. % Cu. This is in relative agreement with the higher crystallization temperature of those compounds than the annealing temperature used in this research (450 ℃). For instance, Cao et al. showed that the crystallization temperature of CuV_2O_6 is between 500 and 550 ℃[40]. The crystallization of a 2nd phase from 17 at. % Cu corresponding

to $BiCu_2VO_6$ (JCPDS No: 089-7016, space group: $P2_1/n$) in small quantities also emerged. In the sample with 23 at. % Cu, the crystallization of the tetragonal $BiVO_4$ phase (t-$BiVO_4$, JCPDS 14-0133, space group: $I4_1/amd$) prevailed on the monoclinic structure. The effect of Cu on the $BiVO_4$ structure was already observed and reported in the literature [41]. The introduction of dopants favors the stabilization of the tetragonal phase [42].

A finer observation of the XRD patterns reveals a slight and progressive decrease of the a and b cell parameters and almost constant c parameter by the increase of the Cu content in the film. This would be the result of the Cu introduction in the monoclinic cell of $BiVO_4$ (in agreement with the lower radius of Cu compared to Bi and V atoms). The calculated cell parameters are provided in **Table. S1**. The relatively small amplitude of the deviation (less than 1 % at 17 at.% Cu) would also be explained by the limited solubility and the formation of an amorphous phase composed of Cu.

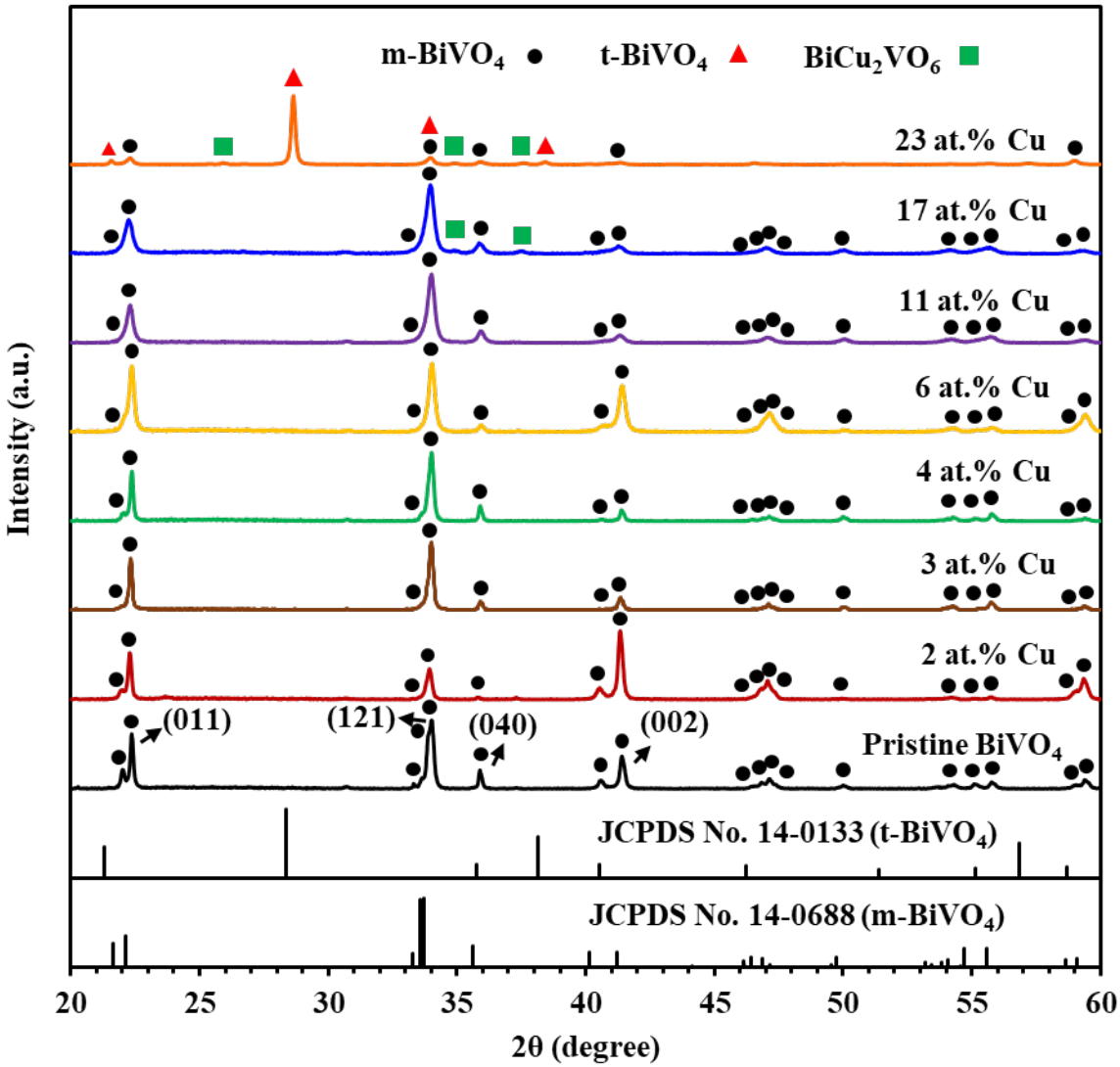

Fig. 1 XRD patterns of the pristine $BiVO_4$ and Cu-incorporated samples.

To compare the influence of the Cu incorporation on the preferential orientation of the samples, the texture grades (TG_{hkl}) corresponding to (011), (121), (040), and (002) as the most intense diffraction lines positioned at 2θ = 22.09, 33.74, 35.63 and 41.14°, respectively, were calculated based on **Eq. 4** [43] using the intensity of the peaks, and the results are presented in **Fig. 2**.

$$TG_{hkl} = \frac{I_{hkl}/I^{s}_{hkl}}{\frac{1}{n}\sum_{i=1}^{n} I_{i(hkl)}/I^{s}_{i(hkl)}} \qquad \textbf{(Eq. 4)}$$

Where I_{hkl}, I^{s}_{hkl} and n, represent the intensity of the corresponding (hkl) diffraction peak, the standard intensity of the peak in the corresponding JCPDS card and the number of planes (n = 4 in our case), respectively. The $TG_{hkl} > 1$ depicts a higher intensity of the corresponding (hkl) diffraction line compared to the standard value reported in the JCPDS card, which represents a preferential orientation along the direction of the corresponding (hkl) plane. The samples demonstrate a relatively high $TG_{(011)}$ value in the range of 1.3 to 2.8, where the highest values are ascribed to the samples with 3 and 4 at % Cu, while $TG_{(121)} < 1$ is true for all the samples, which supposed to be the main peak based on the standard card. What stands out in the graph is the very high $TG_{(002)} > 3$ for the sample with a 2 at. % Cu (and ~2.4 with 6 at. % Cu) suggesting that many crystalline grains were oriented along [002].

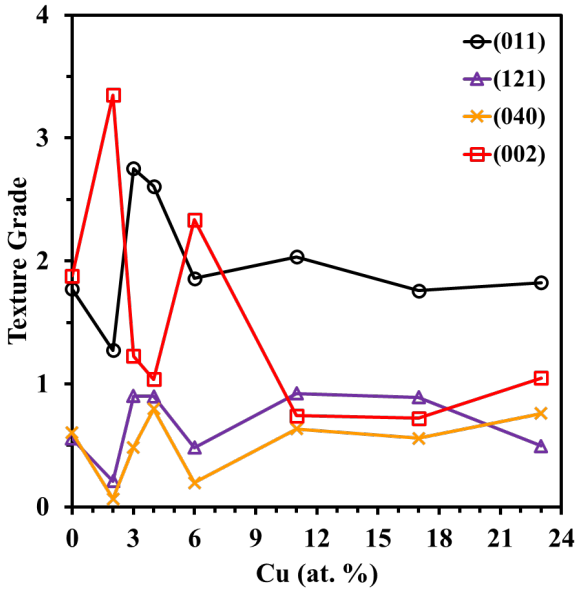

Fig. 2 texture grades of the samples corresponding to (011), (121), (040) and (002) planes.

The top surface FESEM observations of the samples along with the corresponding elemental mappings were provided in **Fig. 3** to investigate the morphology of the thin films, as well as the distribution of the elements. The pristine $BiVO_4$ thin film shown in **Fig. 3** (a) demonstrates a uniform surface with the presence of cracks, which tend to disappear in the Cu-incorporated thin films. The formation of these cracks was previously reported [17] as a result of the difference in the linear expansion coefficient of the film and the substrate coupled with the crystallization. Thus, Cu incorporation seems to decrease the crack density of the $BiVO_4$ thin films and mitigate the crack formation problem. In a higher magnification image shown in **Fig. S2**, nanometric black dots on the film surface could be seen, which represents a nanoporous morphology. These nanopores were caused by the presence of Bi as a low melting element. This phenomena was discussed in previous works [10,17]. The thin film with a 2 at. % Cu shown in **Fig. 3** (b) depicts finer grain size compared to the pristine $BiVO_4$ sample. It also shows shard-like nodules on the surface based on Cu and V elements. The formation of the shards being clearly distinct from the $BiVO_4$ films would be related to a 2^{nd} amorphous phase as supposed from the analyses of XRD. The shards on the sample with a 3 at. % Cu, shown in **Fig. 3** (c), are smaller in size and more numerous on the film surface, while the $BiVO_4$ grains are coarser. The shards on the thin film with a 4 at. % Cu, demonstrated in **Fig. 3** (d), seem to conform more to spherical shapes with a degree of porosity in the $BiVO_4$ phase (black holes). The sample with a 6 at. % Cu shown in **Fig. 3** (e) demonstrates a uniform distribution of the Cu element, which also conforms to the FESEM and elemental mapping observations of the thin films with an 11 and 17 at. % Cu, shown in **Fig. 3** (f) and (g). The thin film with a 23 at. % Cu depicted in **Fig. 3** (h) appears to have a higher porosity

and surface roughness compared to other samples with less Cu content. The shard-like nodules seem to disappear in the thin films with higher than 4 at. % Cu, which could be due to the increased deposition rate as the result of raising the discharge power of the Cu target, leaving less time for the coalescence of the sputtered atoms on the substrate to form shard-like nodules. In a higher magnification shown in **Fig. S2**, it is observable that the thin films enjoy a nanoporous morphology. The brittle fracture cross-section images shown in **Fig. S2** demonstrate the thickness of the films to be in the range of 1 – 1.2 μm.

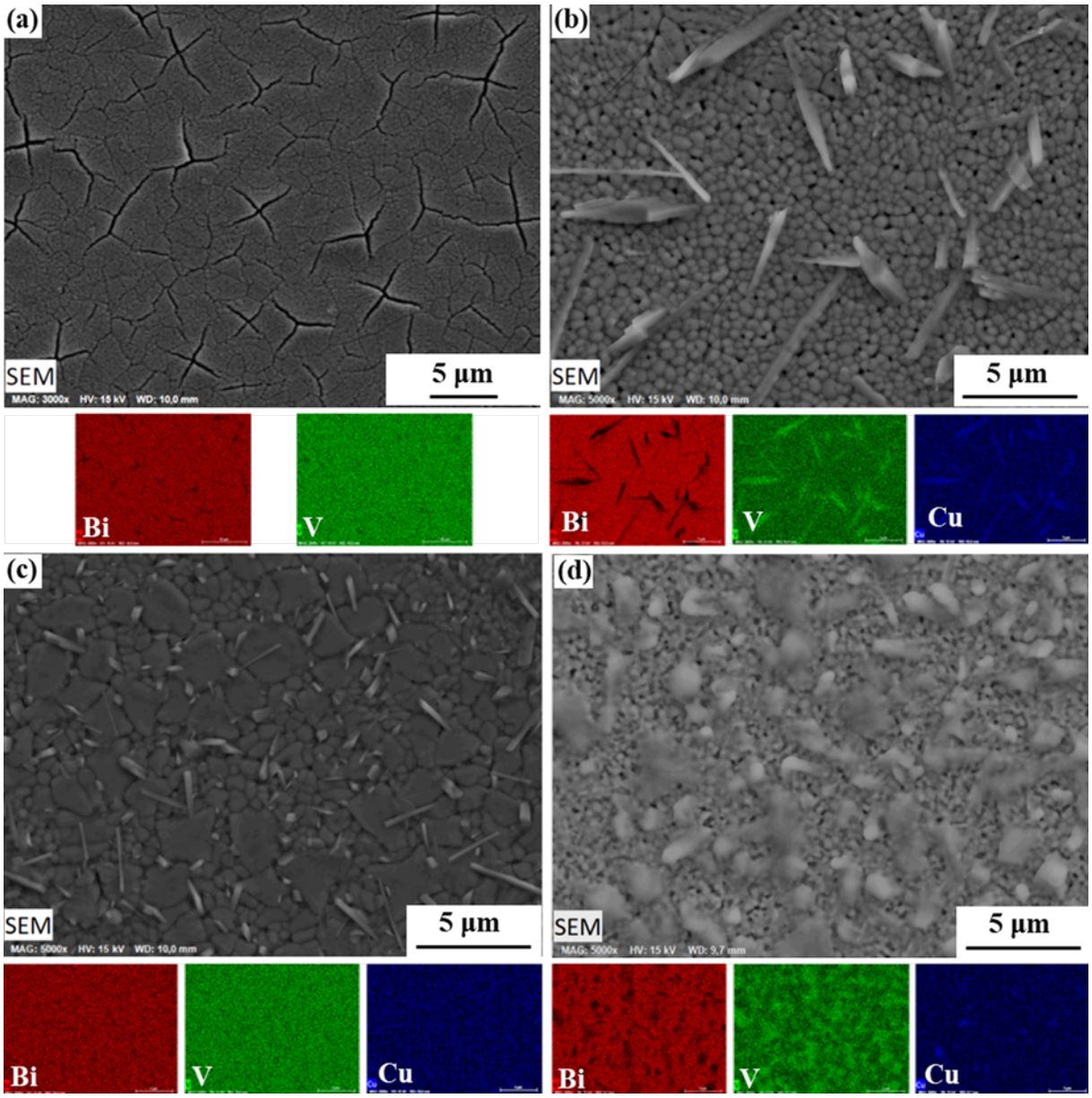
(a)
SEM
MAG: 3000x HV: 15 kV WD: 10,0 mm
5 µm
Bi
V
(b)
SEM
MAG: 5000x HV: 15 kV WD: 10,0 mm
5 µm
Bi
V
Cu
(c)
SEM
MAG: 5000x HV: 15 kV WD: 10,0 mm
5 µm
Bi
V
Cu
(d)
SEM
MAG: 5000x HV: 15 kV WD: 9,7 mm
5 µm
Bi
V
Cu

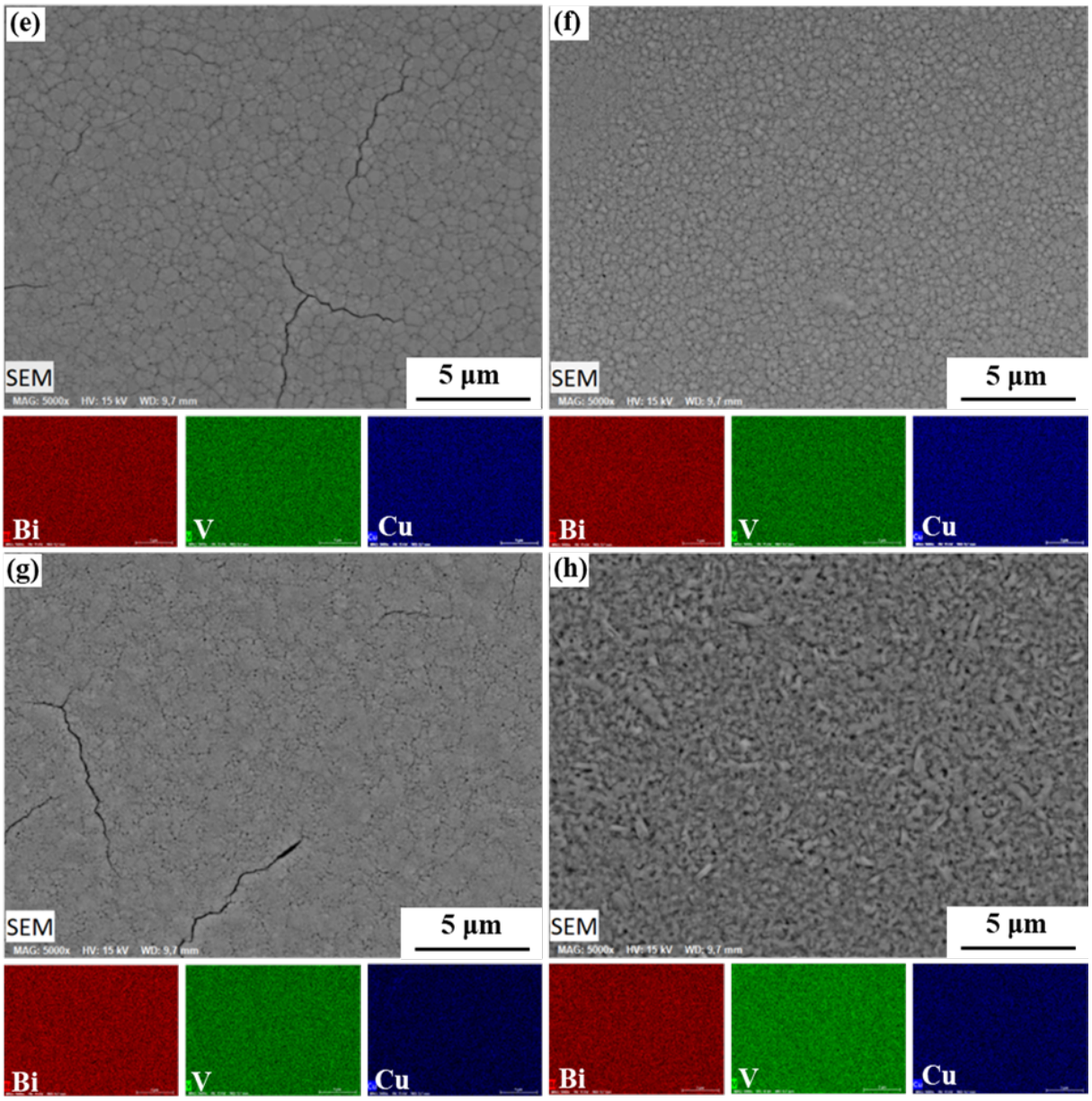

Fig. 3. FESEM and elemental mappings of (a) the pristine $BiVO_4$ sample, and the thin films with a Cu concentration of (b) 2, (c) 3, (d) 4, (e) 6, (f) 11, (g) 17, (h) 23 at. %.

The chemical states of the film surfaces were investigated using the XPS method. The survey spectra of the samples are depicted in **Fig. S3** showing the presence of Bi, V, Cu, O and C elements

on the films' surfaces. The Cu 2p peaks in the spectra become more intense with the rise of Cu at. %. **Fig. 4** (a) exhibits the Cu 2p core levels with peak values at around 933 and 953 eV corresponding to Cu $2p_{3/2}$ and Cu $2p_{1/2}$, respectively. The peaks around 942 and 962 with the shake-up satellite structure were also observed in all the samples which is the characteristic of Cu^{2+} [44,45]. Since the Cu $2p_{3/2}$ peak in the samples with Cu is not unimodal, they could be deconvoluted to multiple components with the maximum at around 932, 934 and 935 eV corresponding to Cu^{+}, Cu^{2+} (oxide) and Cu^{2+} (hydroxide) [44], respectively. The reproduced curve in the deconvolution process is shown in a dotted line. It could be concluded that all the samples are composed of Cu^{2+}/Cu^{+} species with a higher proportion of Cu^{2+}. It is mentioned by Biesinger [44,46] that the shape of the shake-up satellite structure could be used to qualitatively identify the Cu^{2+} species. The shape of the shake-up structure corresponding to the sample with 23 at. % Cu conforms to that of oxide Cu^{2+} which could be verified by the prominent peak at 934 eV. The shake-up structure of the samples with a 17 and 6 at. % Cu resembles that of hydroxide Cu^{+2} presented in the report. The peak intensity at 935 eV was also developed compared to the peak at 934 eV, which verifies that the share of the hydroxide Cu $^{2+}$ rose. It is noteworthy that the Cu^{2+} proportion increases more than that of Cu^{+} with the Cu introduction. It is also possible that Cu^{0} species exist in the samples, but since its peak is very close to that of Cu^{+} [46], it is indistinguishable by the XPS technique, however its probability is very low due to the formation of the 2nd phase based on Cu, V and O as observed by EDS. The Bi 4f core-level spectra are shown in **Fig. 4** (b) with peaks at around 164.5 and 159.3 eV ascribed to Bi $4f_{5/2}$ and Bi $4f_{7/2}$, respectively. It shows the existence of the Bi^{3+} oxidation state associated with the $BiVO_4$ structure. A slight peak shift to lower binding energies was observed in the Bi 4f spectra by the rise of Cu content. It has

been suggested in the literature [47] that the charge transfer and hybridization effect as a result of the penetration of the dopant elements into the crystal could cause a shift in the core level spectra, confirming the Cu introduction into the monoclinic $BiVO_4$ phase as observed from the XRD observations. V $2p_{1/2}$ and V $2p_{3/2}$ peaks at around 524.6 and 516.9 eV are demonstrated in **Fig. 4** (c). It has been reported [48] that V^{5+} and V^{4+} could co-exist in the $BiVO_4$ structure, therefore V $2p_{3/2}$ was deconvoluted to its component peaks at around 516.3 and 516.9–517.1 eV corresponding to V^{4+} and V^{5+}, respectively, which is in agreement with the literature [44,49]. The O 1s peak corresponding to lattice oxygen at around 530 eV could be observed in **Fig. 4** (d). A slight shift is seen in the O 1s spectra probably as a result of Cu incorporation as well. In some samples, a small shoulder at around 533 eV is also noticed which could be ascribed to adsorbed hydroxyl groups [50].

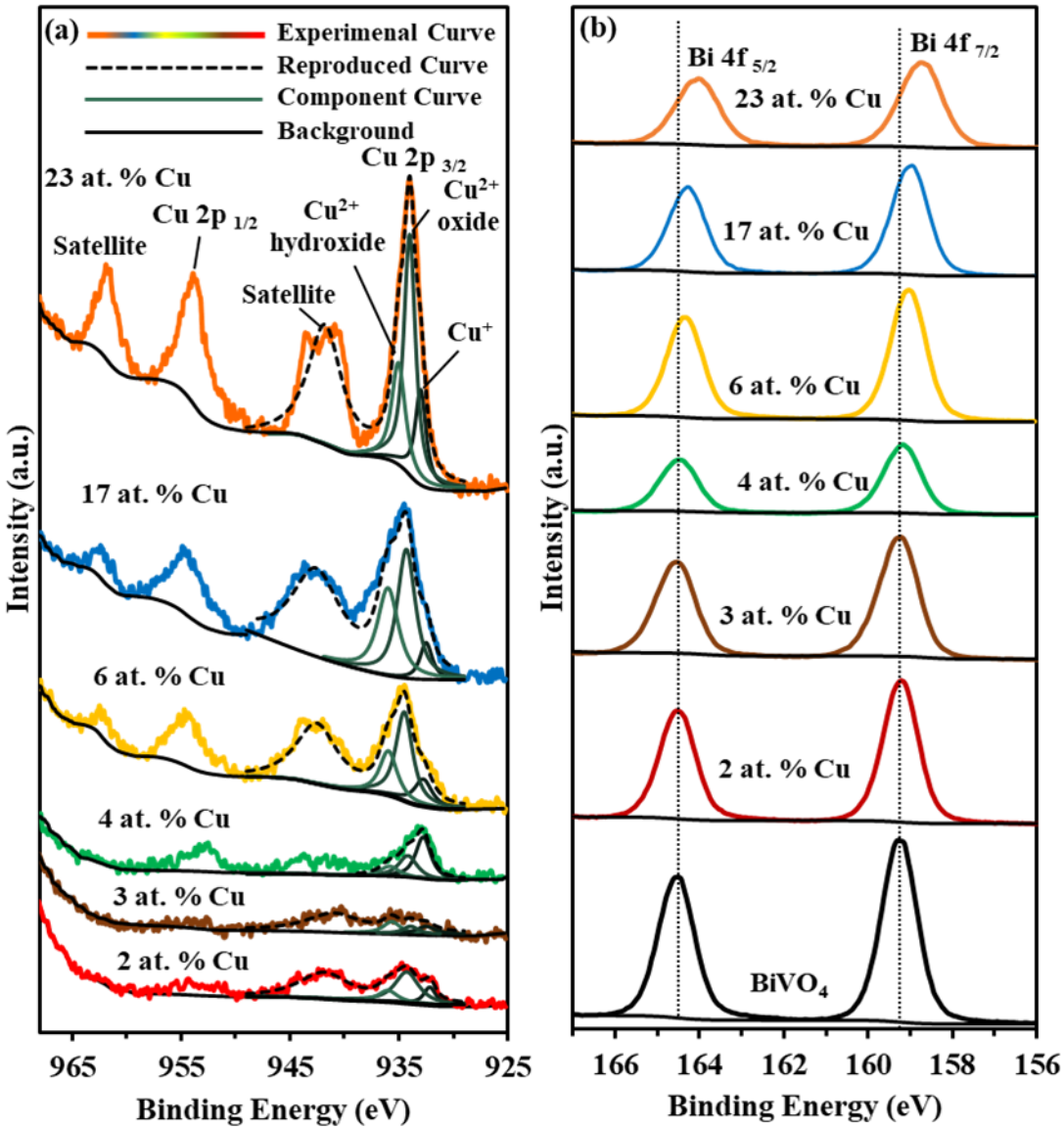
(a)
Experimenal Curve
Reproduced Curve
Component Curve
Background
23 at. % Cu
Cu 2p 3/2
Cu 2p 1/2
Cu2+ oxide
Cu2+ hydroxide
Satellite
Satellite
Cu+
17 at. % Cu
6 at. % Cu
4 at. % Cu
3 at. % Cu
2 at. % Cu
Intensity (a.u.)
965
955
945
935
925
Binding Energy (eV)
(b)
Bi 4f 5/2
Bi 4f 7/2
23 at. % Cu
17 at. % Cu
6 at. % Cu
4 at. % Cu
3 at. % Cu
2 at. % Cu
BiVO4
Intensity (a.u.)
166
164
162
160
158
156
Binding Energy (eV)

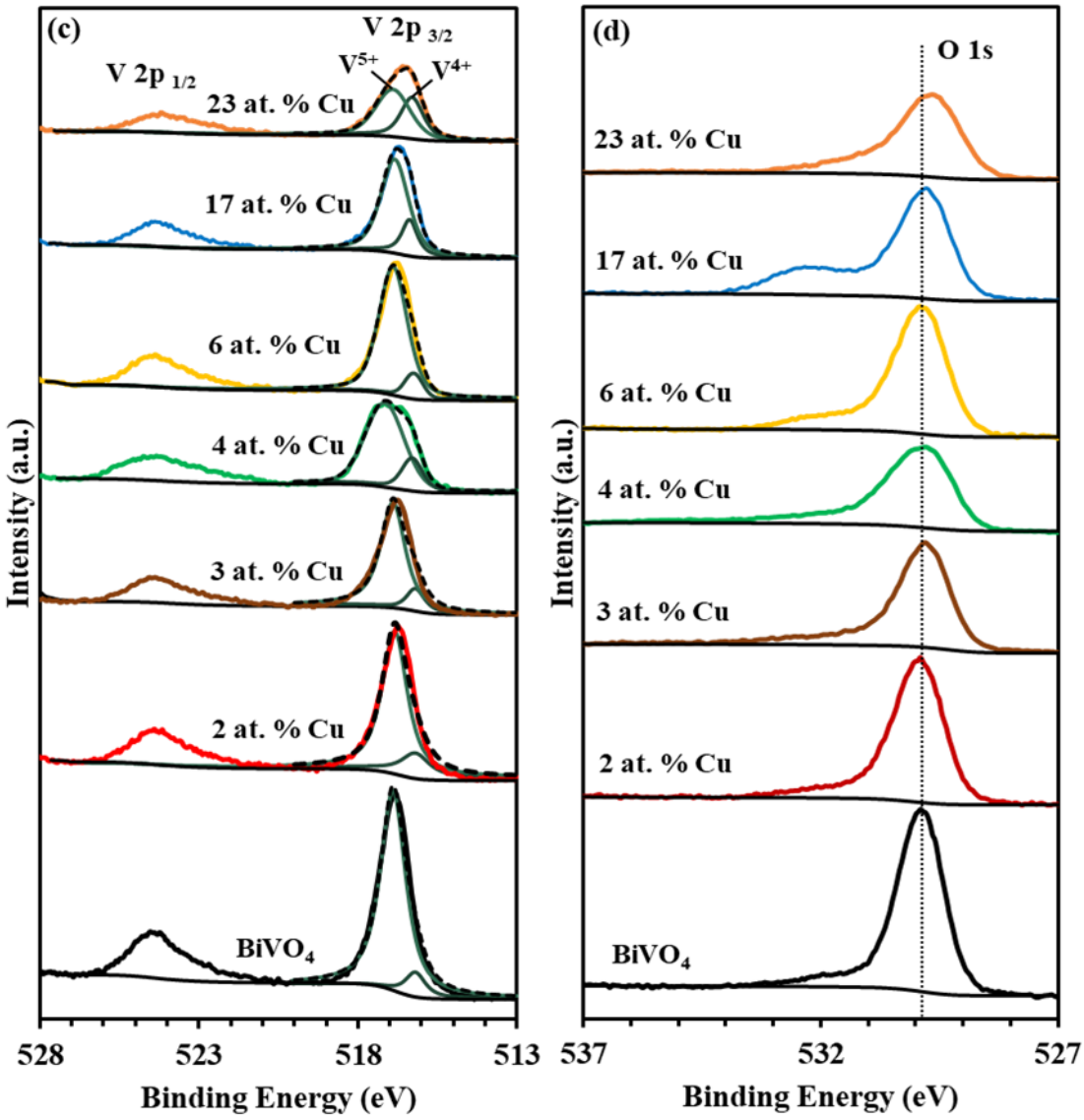

Fig. 4. High-resolution XPS spectra of (a) Cu, (b) Bi, (c) V, (d) O core levels

The ratio of V^{4+}:V^{5+} as a function of the Cu incorporation was calculated and the results are illustrated in **Fig. 5 (a)**. The upward trend of the plot shows the rise of V^{4+}:V^{5+} by increasing the Cu content, indicating the introduction of Cu ions into the $BiVO_4$ structure. It could also be interpreted as the rise of oxygen vacancies due to Cu doping. The valence band XPS (VB-XPS)

technique was employed to measure the valence band edge potential of the samples, and the results are demonstrated in **Fig. 5 (b)**. The energy difference between valence band and the fermi level of the pristine $BiVO_4$ and 2 at. % Cu thin films are 1.94 and 1.65 eV, respectively. The Cu doping caused the potential edge of $BiVO_4$ thin film to be decreased.

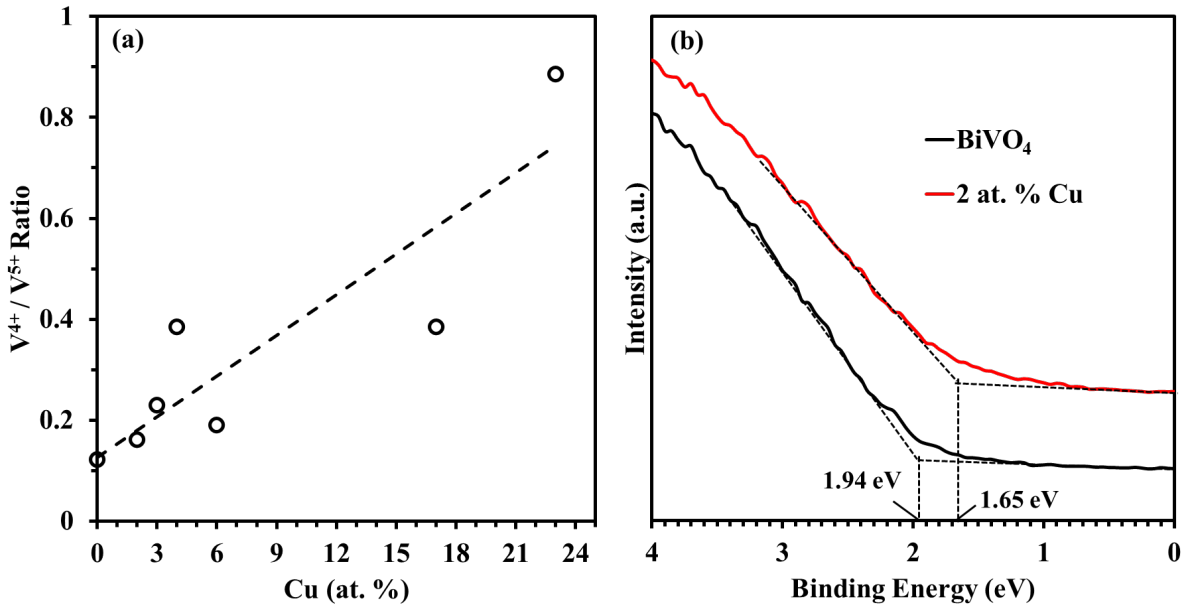

Fig. 5. (a) V^{4+}:V^{5+} versus Cu content and (b) Valence band XPS spectra of pristine $BiVO_4$ and the thin film with a 2 at. % Cu

TEM and HRTEM images of the $BiVO_4$ thin film with 2 at. % Cu incorporation are shown in **Fig. 6.** The interplanar spacings were calculated using the FFT method and demonstrated in HRTEM images with the values of 0.26 and 0.3 nm corresponding to (002) and (121) crystallographic planes based on (JCPDS card No. 14-0688). A large amount of the crystallites in the TEM images are oriented along [002], which is consistent with the texture grade data shown in **Fig. 1** (b). The **Fig. 6** (a) inset graph is showing SAED pattern with discrete spots conforming

to the single crystal pattern, and therefore, each spot could be assigned to a specific crystallographic plane. **Fig. 6** (b), the lack of the lattice fringes in the left side of the HRTEM image marked by the yellow dotted line exhibits the amorphous phase. The inset SAED pattern also demonstrate a mild diffuse ring which is the characteristic of the amorphous structure. This is in agreement with the FESEM observation of the shard-like nodules on the film surface shown in **Fig. 3** (b) that were not observed in the XRD analysis. The heterostructure interface between m-$BiVO_4$ and Cu-O-V amorphous phase is distinguished by the yellow dotted line in the images, which could facilitate the charge carrier separation. The elemental EDS analysis corresponding to the area shown in **Fig. 6** (b) is also provided and depicted in **Fig. 6** (c). The selected area consists of 27.3 at. % Cu, which verifies the presence of the Cu-based phase observed before in XRD and FESEM in this area proving the amorphous structure of the Cu-O-V as the secondary phase.

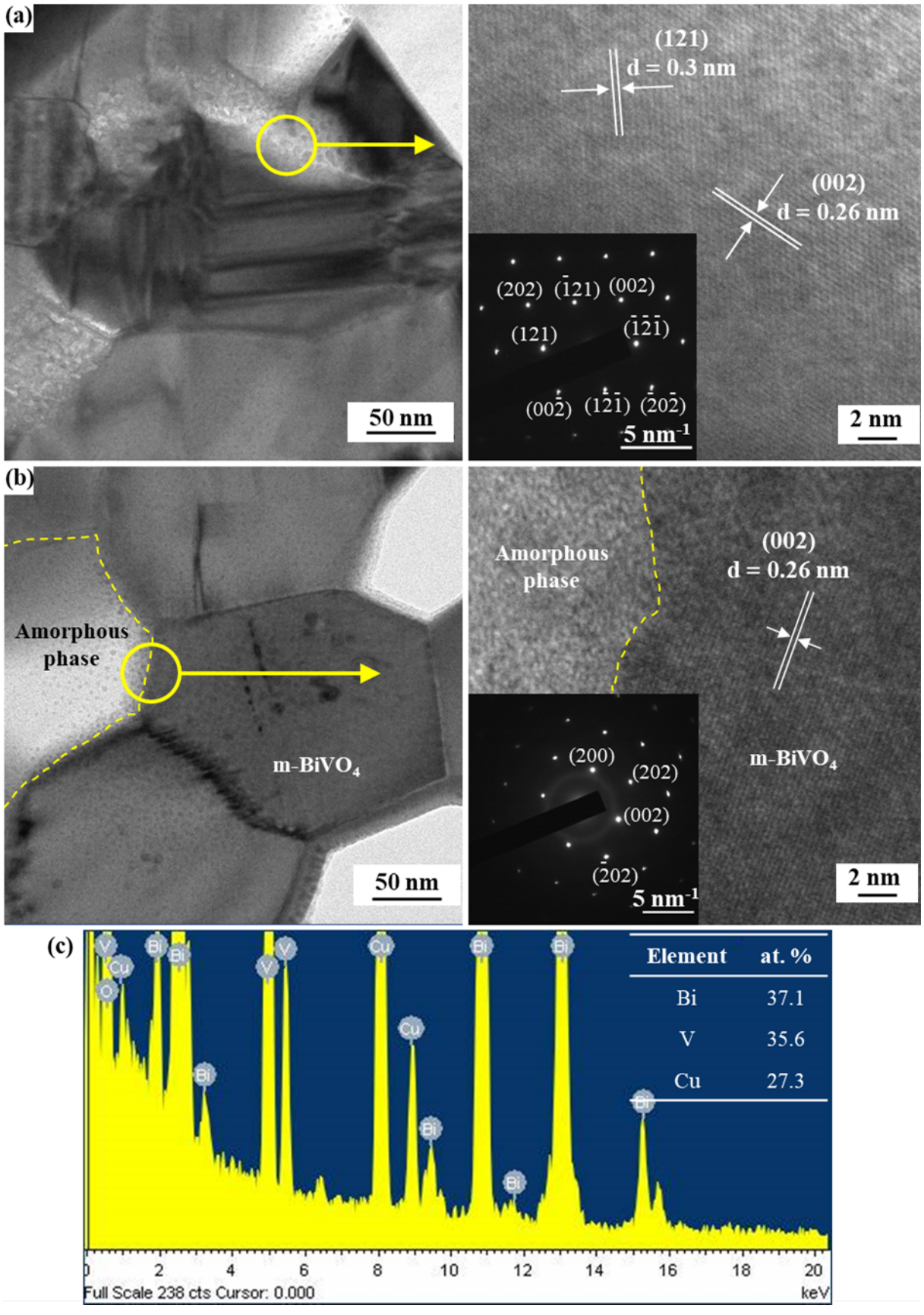
(a)
50 nm
(121)
d = 0.3 nm
(002)
d = 0.26 nm
(202) (1̄21) (002)
(121)
(1̄2̄1̄)
(00 2̄) (12̄1̄) (2̄02̄)
5 nm-1
2 nm
(b)
Amorphous phase
m-BiVO4
50 nm
Amorphous phase
(002)
d = 0.26 nm
(200)
(202)
(002)
(2̄02)
5 nm-1
m-BiVO4
2 nm
(c)
V
Cu
O
Bi
Bi
V
V
Cu
Bi
Bi
Cu
Bi
Bi
Bi
Element at. %
Bi 37.1
V 35.6
Cu 27.3
0 2 4 6 8 10 12 14 16 18 20
Full Scale 238 cts Cursor: 0.000
keV

Fig. 6. (a), (b) TEM and HRTEM images of $BiVO_4$ thin film with 2 at. % Cu incorporation with SAED patterns, and (c) elemental EDS analysis providing at. % of the corresponding image.

3.2. Optical properties

The absorbance spectra depicted in **Fig. 7** (a) were calculated based on **Eq. 1** using transmittance and reflectance spectra measured by UV-Vis spectrophotometry (see **Fig. S4**). The absorbance spectra show the absorption edge of the pristine $BiVO_4$ at around 490 nm, which agrees with the literature data [51,52]. The spectra corresponding to Cu-incorporated thin films are also in close range with that of the pristine $BiVO_4$, except for the film with 23 % at. Cu exhibiting a lower absorption coefficient below 500 nm. The bandgap of the samples calculated by the Tauc plot method is illustrated in **Fig. 7** (b), and the bandgap values versus Cu contents of the thin films are shown in **Fig. 7** (c). The bandgap of the pristine $BiVO_4$ thin film is calculated to be 2.5 eV and those of the Cu-incorporated samples are in the range of 2.5–2.6 eV. The variation of the bandgaps could stem from the Cu doping or emerging of the 2nd phase. The sample with a 23 at. % Cu showed a lower bandgap (2.46 eV) due to the crystallization of the $BiCu_2VO_6$ secondary phase with a lower bandgap value of 2.1 eV [53]. It also exhibits a secondary absorption edge around 450 nm that could well be ascribed to the t-$BiVO_4$ phase with bandgap value of 2.9 eV [54]. The change in the morphology and porosity of the thin films increased the reflectance around 600 nm, shown in **Fig. S4** (b) by increasing the diffuse reflectance component.

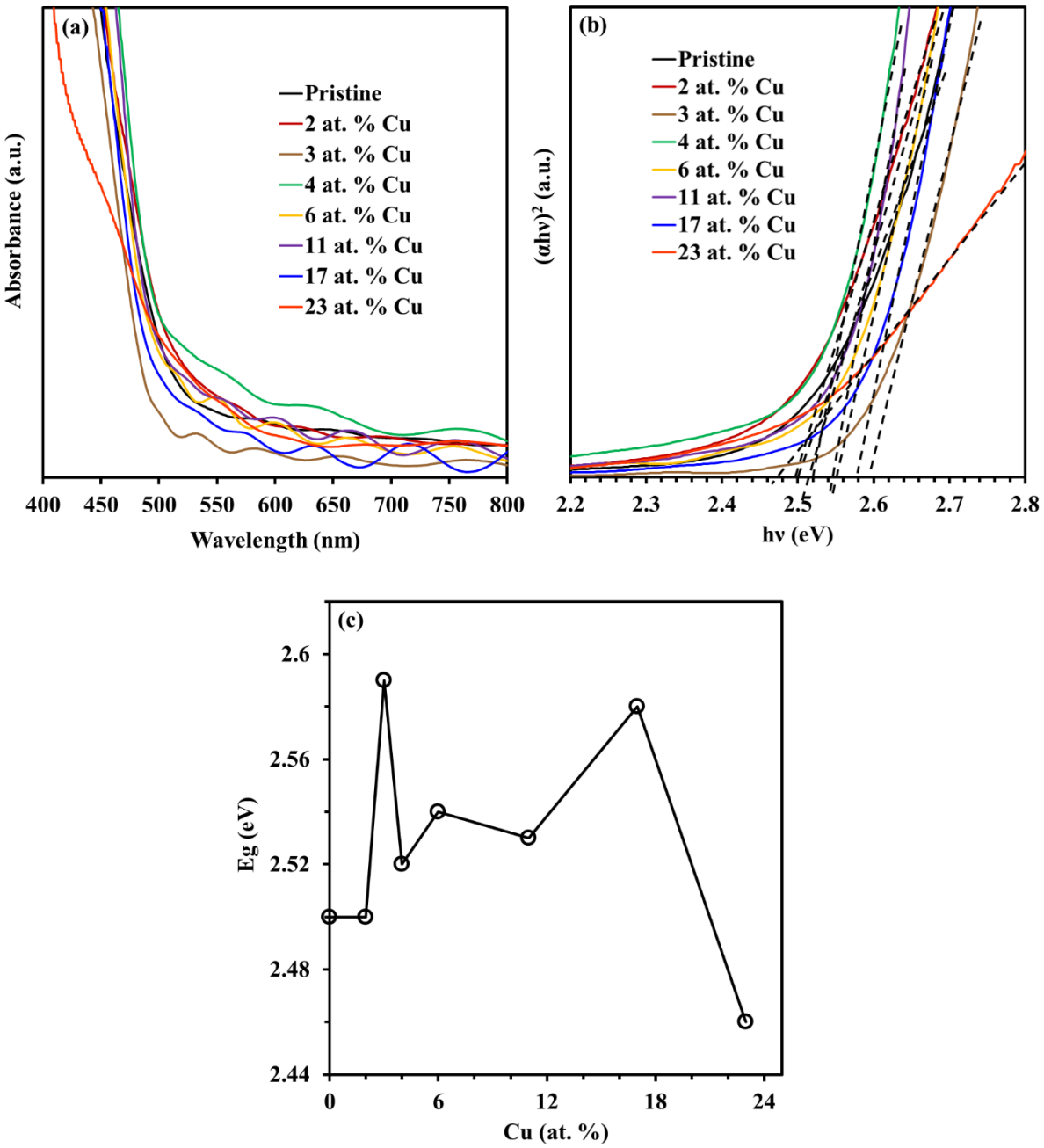

Fig. 7. (a) Absorbance spectra of the thin films with various Cu content (b) Tauc plots of the samples, and (c) bandgap values of the samples vs at. % Cu.

3.3. Photocatalytic activity

The visible-light-driven photocatalytic activity of the Cu-incorporated thin films was investigated through the RhB photodegradation experiments at neutral pH (7), and the results are illustrated in **Fig. 8** (a). The kinetics results based on the pseudo-first-order model given by **Eq. 3** are provided in **Fig. S5** (a), and the rate constants representing the photocatalytic potential in the corresponding photoreaction are demonstrated in the inset graph of **Fig. 8** (a). The blank experiment was conducted to separate the photolysis effect. The dark experiment for each sample was performed for 60 min and the solutions were sampled at 15 min intervals to ensure the system has reached the adsorption-desorption equilibrium. The system reached an equilibrium between 15 to 45 min in all the experiments, and the concentration remained constant after 45 min. Based on these results, the dark section of the photocatalytic experiments in the next stages was performed for 45 min. Herein, the highest photoactivity among the samples is ascribed to the sample with the least amount of Cu content (2 at. %) with a 72 % RhB photodegradation ($k' = 0.19$ h^{-1}). A further increase of the Cu content leads to a progressive decrease of photodegradation. The thin films containing less or equal to 6 at. % Cu performed higher activities (59–72 % RhB photodegradation, $k' = 0.13–17$ h^{-1}) compared to the pristine $BiVO_4$ (54 % RhB photodegradation, $k' = 0.11$ h^{-1}), while the samples with higher than 6 at. % Cu contents showed poorer performance. The photocatalytic performance of the thin films with less than 2 at. % Cu is currently unknown since reaching a composition with a lower amount of Cu using the sputtering machine in this research is challenging. The photocatalytic enhancement could be the result of Cu doping that was verified by the XPS and XRD results, as well as the heterostructure of the crystalline m-$BiVO_4$ and amorphous Cu-O-V phase exhibited in TEM observations, which acts through charge carrier separation inhibiting the fast recombination of photogenerated electrons and holes. The benefits

of employing amorphous materials in the crystalline/amorphous heterostructure have been previously reported [55] owing to providing a more uniform dispersion of active sites, as well as enjoying high unsaturated sites that facilitate the adsorption and surface reactions. Gue et al. reported similar photocatalytic improvement for the mixture of crystalline/amorphous heterostructure of TiO_2/ZnO in H_2 production due to a superior electrical charge separation [56]. Indeed Cu doping could increase the charge carrier concentration, though, the higher amount of Cu incorporation results in fewer active sites on the film surface, subsequently less photoactivity due to the presence of less active phase. The PL results of the Cu-incorporated $BiVO_4$ (2 at. % Cu) and the pristine sample are shown in **Fig. 8** (b). The intensity of the PL spectra could be associated with the recombination rate of the photogenerated electrons and holes [57]. The PL results verified that less recombination occurs in the thin film with a 2 at. % Cu compared to the pristine sample. Cu dopants could function as electron traps by creating electronic states below conduction band and receiving electrons changing their oxidation states from Cu^{2+} to Cu^{+} and Cu^{+} to Cu^{0} [58], hence inhibiting the recombination and providing more time for photogenerated charge carriers to participate in the redox reactions to destroy organic pollution.

The scavengers experiment using trapping agents of reactive species could help to study the photocatalytic mechanism by identifying the reactive agents acting the main role in the RhB photodegradation process under visible light by Cu-incorporated $BiVO_4$ thin films. The RhB photodegradation results involving the scavengers, using the sample with the highest photocatalytic activity (2 at. % Cu) from the previous section, are illustrated in **Fig. 8** (c). The photodegradation versus time and the kinetics study are provided in **Fig. S5** (b). The experiment with p-BQ as the trapping agent of superoxide ($^{\bullet}O_2^{-}$) showed a moderate decrease in the

performance by 11 %, while the performance concerning the CN experiment as the electron scavenger experienced a distinctly more decrease of 26 %. This could mean that a significant part of the electrons separately participated in the direct photoreduction of RhB. This phenomenon has been reported in the literature [59] and also observed by our team [10] regarding the photocatalytic degradation of RhB by pristine $BiVO_4$ thin films. The contribution of electrons in pristine $BiVO_4$ is lower than that implied in the Cu-doped $BiVO_4$ film, probably resulting from a direct effect of Cu doping on the electron charge carrier concentration. Electrons could also contribute to photodegradation through the reduction of superoxide radicals producing hydrogen peroxide (H_2O_2) through **Eq. 7** [60]. The results of EDTA (36 %) and Methanol (44 %) experiments as the scavengers of the photogenerated holes (h^+) and hydroxyl radicals ($^{\bullet}OH$), respectively demonstrate the vital role of these reactive agents. This is in agreement with the electron paramagnetic resonance results published in the literature for Cu-doped $BiVO_4$ photocatalyst with 0.75 % Cu incorporation showing the production of $^{\bullet}OH$ radicals and its importance in the photodegradation of organic pollutants [61]. Based on the collective results in this part, it could be stated that a part of the hydroxyl radicals involved in the photodegradation process was produced by the oxidation of hydroxide ions (OH^-) through **Eq. 5** and the rest were produced through the reduction of superoxides described by **Eq. 6 – 8**. The Haber-Weiss reaction (**Eq. 8**) is a well-known path for producing hydroxyl radicals in photocatalysis [60]. Based on the results illustrated in **Fig. 8** (c), it could be concluded that the photogenerated holes have a crucial role in the RhB photodegradation mechanism, as well as the hydroxyl radicals.

$$OH^- + h^+ \rightarrow {}^{\bullet}OH \qquad \textbf{(Eq. 5)}$$

$$O_2 + e^- \rightarrow {}^{\bullet}O_2^- \qquad \textbf{(Eq. 6)}$$

$$^{\bullet}O_2^- + 2H^+ + e^- \rightarrow H_2O_2 \quad \textbf{(Eq. 7)}$$

$$H_2O_2 + {}^{\bullet}O_2^- \rightarrow {}^{\bullet}OH + O_2 + OH^- \quad \textbf{(Eq. 8)}$$

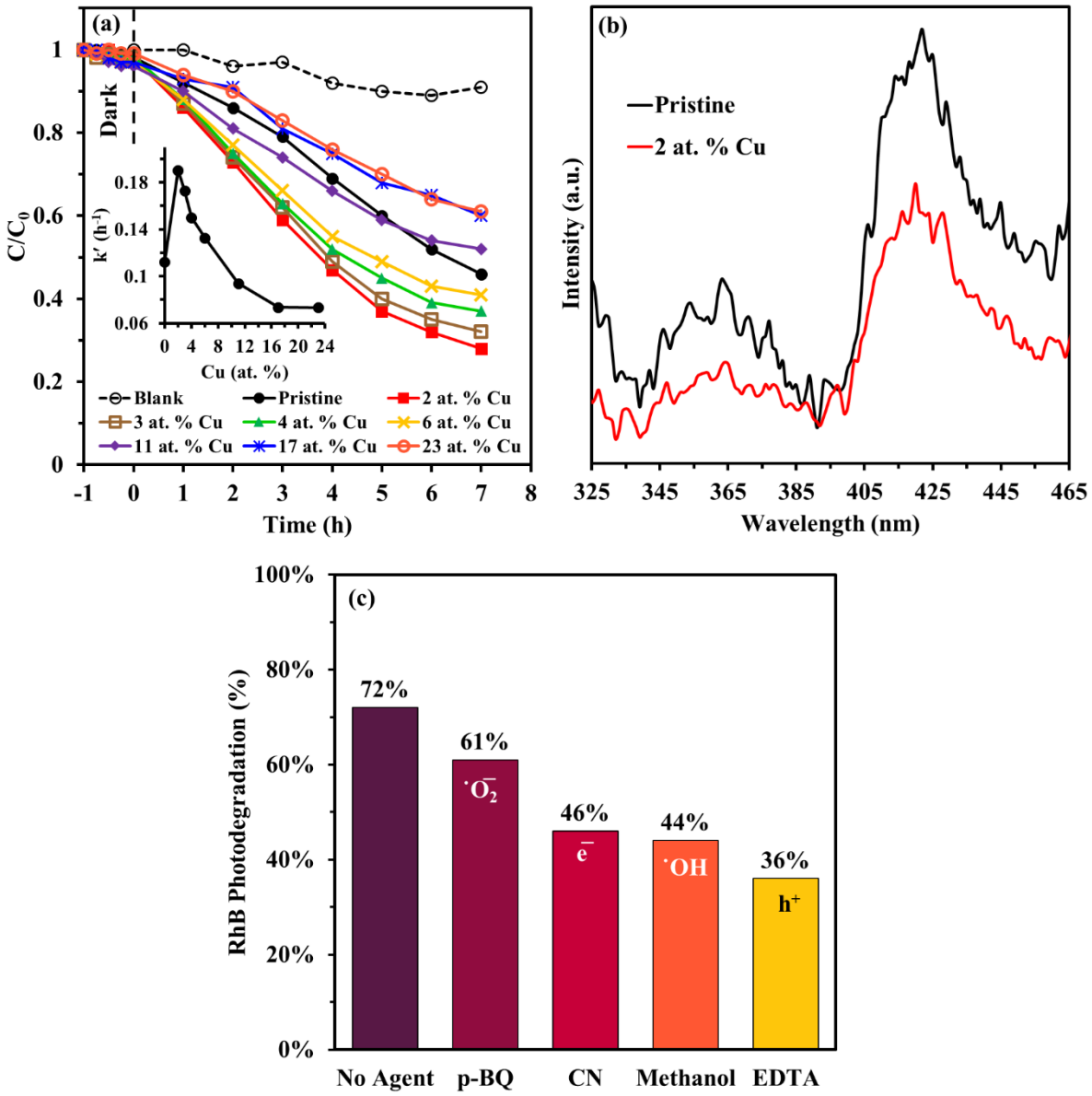

Fig. 8 (a) RhB photodegradation experiments of Cu-incorporated samples at pH = 7 and the inset graph shows the rate constants of the photoreactions vs Cu content, (b) the PL spectra of the pristine $BiVO_4$ and the thin film with a 2 at. % Cu, (c) photocatalytic experiments involving the scavengers by the thin-film photocatalyst with a 2 at. % Cu

Recyclability and reusability are parts of the most important advantages of thin-film photocatalysts, therefore a recycling experiment could verify the stability of the thin films after exploitation. Three consecutive cycles of RhB photodegradation by the thin film with a 2 at. % Cu was performed under visible light at neutral pH. The results presented in **Fig. 9** (a) show a slight decrease in the performance by only 4 % after 3 × 7 h of photocatalytic exploitation under visible light. The XRD pattern of the samples before and after the recycling experiment demonstrated in **Fig. 9** (b) verifies the stability of the $BiVO_4$ structure after the photodegradation process. It is also in agreement with a previous study of our team on the recyclability of the pristine $BiVO_4$ thin films deposited by reactive magnetron sputtering [10]. The results of this section proves the consistent performance of the Cu-doped $BiVO_4$ thin-film photocatalysts.

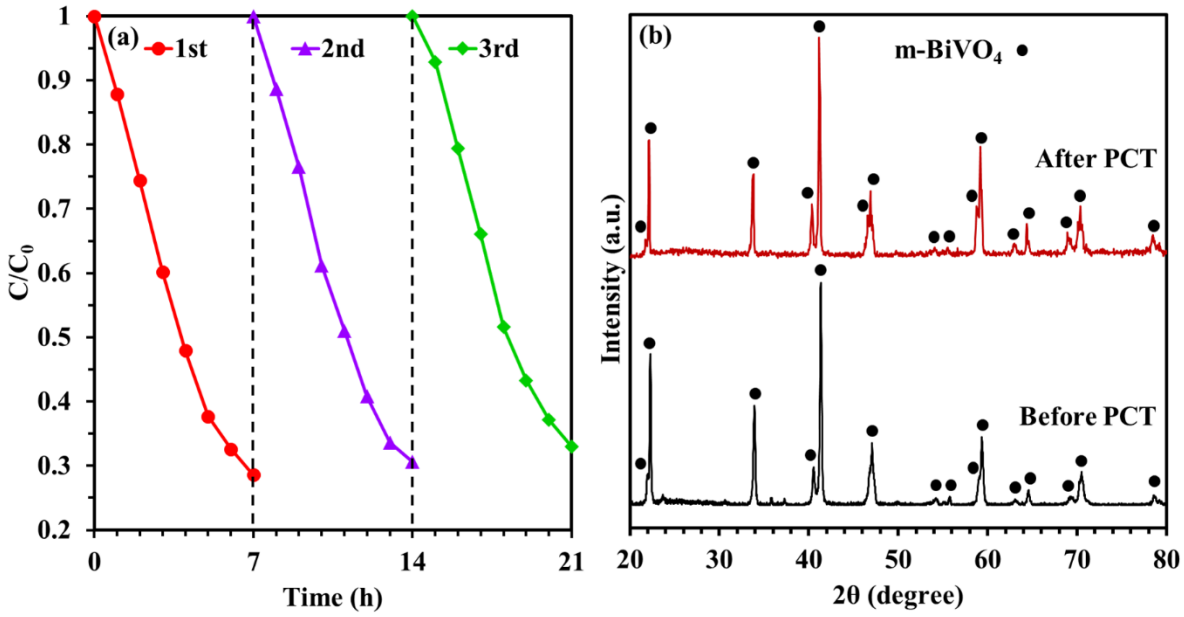

Fig. 9 (a) recycling experiment in three consecutive cycles of RhB photodegradation by the thin film with a 2 at. % Cu and (b) XRD pattern of the samples before and after the recycling experiment

The RhB photodegradation by the Cu-incorporated $BiVO_4$ thin films was investigated in the previous sections. It could also be advantageous to examine the photocatalytic performance involving other organic dyes with various anionic and cationic characteristics such as MO and MB, respectively. Therefore, the visible-light-driven photodegradation of RhB, MB and MO at neutral pH by the pristine $BiVO_4$ thin film and the one with a 2 at. % Cu were compared, and the results are illustrated in **Fig. 10** (a), and the corresponding photodegradation versus time and the kinetics of the photoreactions are provided in **Fig. S6** (a) and (b), respectively. Cu-incorporated $BiVO_4$ thin film with a 2 at. % Cu showed higher photoactivity in all cases with 72 % ($k' = 0.19\ h^{-1}$), 85 % ($k' = 0.28\ h^{-1}$) and 51 % ($k' = 0.1\ h^{-1}$) for RhB, MB and MO, respectively, compared to the pristine sample with 54 % ($k' = 0.11\ h^{-1}$), 61 % ($k' = 0.13\ h^{-1}$) and 28 % ($k' = 0.05\ h^{-1}$) photodegradation, exhibiting the superior photocatalytic performance of Cu-incorporated $BiVO_4$ towards the photodegradation of organic dye pollutions. The photodegradation towards MB was performed with highest efficiency followed by RhB and MO. One reason could be the cationic/anionic nature of the dyes. The photocatalytic degradation of organic dye pollutions occurs stepwise. Firstly, the dye molecules are adsorbed on the surface of the photocatalyst, and secondly, the degradation happens on the surface through the redox reactions previously discussed. Therefore, the adsorption property of the photocatalyst is of great importance. It is reported in the literature that the point of zero charges (pH_{pzc}) of $BiVO_4$ is around 2.5 [62]. Thus, assuming the

small amount of Cu content (2 at. %) has a negligible impact on the PZC shift, the surface of the thin film is negatively charged at pH = 7, and therefore, due to electrostatic charges, has a stronger attraction towards a cationic dye (MB) rather than an anionic dye (MO) or a dye with a neutral charge at pH = 7 (RhB). The adsorption values concerning each dye in the dark experiment, depicted in **Fig. S7**, also support this with a 5.1 % decrease in the concentration for MB compared to 3 and 2 % for MO and RhB, respectively at pH = 7. The lowest unoccupied molecular orbital (LUMO) and the highest occupied molecular orbital (HOMO) of the dyes are provided in **Fig. 10** (c), as well as the band edge position of the Cu-incoporated $BiVO_4$ photocatalyst gathered from VB-XPS shown in **Fig. 5** (b), and the spectrophotometry analysis. The LUMO of RhB (0.54 V vs RHE) [63] is more positive than that of MO (− 0.036 V vs RHE) [63] and MB (0.065 V vs RHE) [63], hence, in addition to the previous argument regarding the surface adsorption, it should be noted that the photo-oxidation of the RhB dyes could be more difficult compared to other dyes. Plus, since the reduction potential of H_2O_2 (0.32 V) [64] produced during redox reactions (**Eq. 7**) is lower than RhB LUMO but more positive than that of MB, it could photodegrade MB but not RhB, therefore, it could be considered as another reason for the higher performance of photocatalytic degradation towards MB.

In previous sections, the photocatalytic performance of the samples at neutral pH was investigated. Examining the samples' photoactivity in acidic and basic conditions is also helpful. Therefore, the experiments at pH = 3 and 10 were also conducted. The order of photodegradation efficiency towards different dyes at acidic and basic pH conditions shown in **Fig. 10** (b) along with kinetics studies in **Fig. S6** (c) and (d), are also coherent with that of neutral pH, though, higher photocatalytic activities have been achieved with 100 % ($k' = 0.87\ h^{-1}$) and 99 % ($k' = 0.72\ h^{-1}$)

MB photodegradation, 95 % ($k' = 0.46\ h^{-1}$) and 76 % ($k' = 0.22\ h^{-1}$) RhB photodegradation, and 63 % ($k' = 0.15\ h^{-1}$) and 58 % ($k' = 0.13\ h^{-1}$) MO photodegradation in acidic and basic pH, respectively by the thin film with a 2 at. % Cu. As mentioned before, the pH_{pzc} of $BiVO_4$ is around 2.5, and therefore, at pH = 3 it is negatively charged, while the dye molecules are protonated due to excessive H^+ concentration of the solution, thus more electrostatic attractions could lead to better adsorption of the dye molecules on the photocatalyst surface, where the photoreaction takes place. Moreover, the extra H^+ could result in higher production of the reactive species such as hydrogen peroxide and hydroxyl radical through **Eq. 7** and **8** and enhance the photocatalytic performance [20]. This is also true for the presence of extra OH^- in the basic solution to produce other types of reactive agents through redox reactions based on **Eq. 5 – 8**.

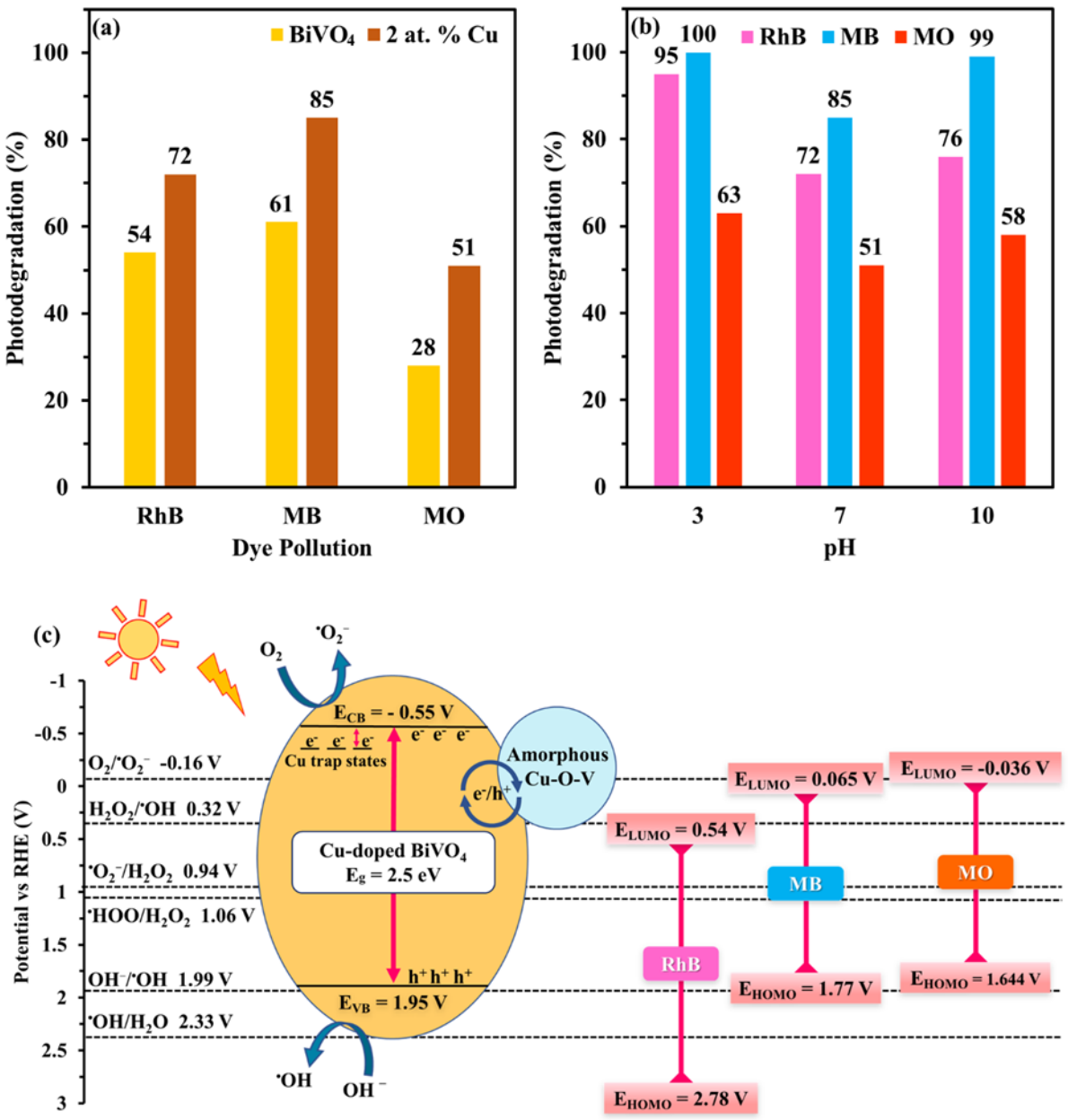

Fig. 10. Visible-light-driven photodegradation of RhB, MB and MO (a) by the pristine $BiVO_4$ and 2 at. % Cu samples at neutral pH, (b) at pH = 3, 7 and 10 by the sample with 2 at. % Cu and (c) the schematic of potentials of organic dyes and the semiconductor sample with a 2 at. % Cu.

A summary of the photocatalytic results achieved in this research and those published in the literature is gathered in the **Table. 2**. The powder form was considerably favored by the researchers, while thin films have many advantages that could not be overlooked like recyclability, reusability and low precursor consumption. This comparison shows that the performance of Cu-doped $BiVO_4$ thin films deposited by reactive magnetron sputtering in this research with high photocatalytic activity could be considered as a proper alternative to powder-form photocatalysts overcoming inherent limitations of powder and provide a viable wastewater treatment operation under sunlight.

Table. 2. Summary of $BiVO_4$ photocatalysts' performance towards photodegradation of organic pollutants.

Photocatalyst	Form	Pollutant	Light source	Degradation efficiency (%)	Ref.
$Cu/BiVO_4$	Powder	MB, 50 mg/L	400 W Xenon	50	[28]
$Cu/BiVO_4$	Powder	RhB, 15 mg/L	250 W Halogen	96	[48]
$Cu/BiVO_4$	Powder	MO, 10 mg/L	54 W LED	86	[65]
$BiVO_4$	Thin Film	Bisphenol-A, 10 mg/L	150 W Xenon	10	[66]
$Y/BiVO_4$	Thin Film	RhB, 0.2 mg/L	300 W Xenon	18	[67]
Ag, Ni, $Co/BiVO_4$	Powder	MB, 10 mg/L	500 W Xenon	90	[68]
$Cu/BiVO_4$	Thin Film	RhB, MB, MO, 5 mg/L	400 W Metal Halide	RhB=95, MB=100, MO=63	This work

4. Conclusions

- Cu incorporation was successfully implemented into nanoporous $BiVO_4$ thin films using reactive magnetron sputtering resulting in enhanced visible-light-driven photocatalytic activity with 100, 99 and 63 % photodegradation of MB, RhB and MO, respectively.
- Cu incorporation affected the preferential orientation of the thin film's crystal structure with a tendency along [002] and [011], particularly concerning the thin film with a 2 at. % Cu. It was observed in HRTEM images that the crystal orientation of the (002) plane is significant. Cu incorporation also affected the cell volume which was progressively decreased and consistent with the lower ion radius of Cu compared to V and Bi.
- Amorphous shard-like Cu-O-V nodules were formed on the Cu-incorporated thin film with a 2 at. % Cu, which were also observed in HRTEM images. They might also promote an effective separation of charge carriers, which was verified by the PL results showing less recombination rate after the Cu incorporation.
- Cu-incorporated $BiVO_4$ with a 2 at. % Cu had a bandgap of 2.5 eV and the XPS results showed the presence of Cu^{+} and Cu^{2+} species. XPS also showed the rise of V^{4+}/V^{5+} by increasing Cu content and verified the penetration of Cu ions into the $BiVO_4$ crystal.
- Hydroxyl radical and photogenerated electrons were identified as the main reactive species driving the RhB photodegradation by the Cu-incorporated $BiVO_4$ thin films under visible light.
- Recyclability experiment with three consecutive cycles proved the films' suitable stability, which will contribute to an effective, cost-efficient and economically viable solution for the industrial water treatment application.

Conflict of interest

The authors declare that they have no conflict of interest.

Acknowledgments

The authors would like to acknowledge the support of this study by the Iran National Science Foundation (project No: 98001285), Pays de Montbéliard Agglomération, and the Iran Nanotechnology Initiative Council for the support of this work.

References

[1] J.J. Rueda-Marquez, I. Levchuk, P. Fernández Ibañez, M. Sillanpää, A critical review on application of photocatalysis for toxicity reduction of real wastewaters, J Clean Prod. 258 (2020) 120694. https://doi.org/10.1016/j.jclepro.2020.120694.

[2] C. Feng, Z. Wu, K. Huang, J. Ye, H. Zhang, Surface Modification of 2D Photocatalysts for Solar Energy Conversion, Advanced Materials. 34 (2022) 2200180. https://doi.org/10.1002/adma.202200180.

[3] C. Feng, L. Tang, Y. Deng, J. Wang, Y. Liu, X. Ouyang, H. Yang, J. Yu, J. Wang, A novel sulfur-assisted annealing method of g-C3N4 nanosheet compensates for the loss of light absorption with further promoted charge transfer for photocatalytic production of H2 and H2O2, Appl Catal B. 281 (2021) 119539. https://doi.org/10.1016/j.apcatb.2020.119539.

[4] O. Akhavan, M. Choobtashani, E. Ghaderi, Protein degradation and RNA efflux of viruses photocatalyzed by graphene-tungsten oxide composite under visible light irradiation, Journal of Physical Chemistry C. 116 (2012) 9653–9659. https://doi.org/10.1021/jp301707m.

[5] S. Ahadi, N.S. Moalej, S. Sheibani, Characteristics and photocatalytic behavior of Fe and Cu doped TiO2 prepared by combined sol-gel and mechanical alloying, Solid State Sci. 96 (2019) 105975. https://doi.org/10.1016/j.solidstatesciences.2019.105975.

[6] E. Montakhab, F. Rashchi, S. Sheibani, Modification and photocatalytic activity of open channel TiO2 nanotubes array synthesized by anodization process, Appl Surf Sci. 534 (2020) 147581. https://doi.org/10.1016/j.apsusc.2020.147581.

[7] G.G. Nakhate, V.S. Nikam, K.G. Kanade, S. Arbuj, B.B. Kale, J.O. Baeg, Hydrothermally derived nanosized Ni-doped TiO2: A visible light driven photocatalyst for methylene blue degradation, Mater Chem Phys. 124 (2010) 976–981. https://doi.org/10.1016/j.matchemphys.2010.08.007.

[8] J. Wang, X. Yang, J. Chen, J. Xian, S. Meng, Y. Zheng, Y. Shao, D. Li, Photocatalytic activity of novel Ag4V2O7 photocatalyst under visible light irradiation, Journal of the American Ceramic Society. 97 (2014) 267–274. https://doi.org/10.1111/jace.12639.

[9] R. Venkatesan, S. Velumani, K. Ordon, M. Makowska-Janusik, G. Corbel, A. Kassiba, Nanostructured bismuth vanadate (BiVO4) thin films for efficient visible light photocatalysis, Mater Chem Phys. 205 (2018) 325–333. https://doi.org/10.1016/j.matchemphys.2017.11.004.

[10] S. Bakhtiarnia, S. Sheibani, A. Billard, H. Sun, E. Aubry, M.A.P. Yazdi, Enhanced photocatalytic activity of sputter-deposited nanoporous BiVO4 thin films by controlling film thickness, J Alloys Compd. 879 (2021) 160463. https://doi.org/10.1016/j.jallcom.2021.160463.

[11] Z. Zhou, J. Chen, Q. Wang, X. Jiang, Y. Shen, Enhanced photoelectrochemical water splitting using a cobalt-sulfide-decorated BiVO4 photoanode, Chinese Journal of Catalysis. 43 (2022) 433–441. https://doi.org/10.1016/S1872-2067(21)63845-7.

[12] H. Bai, F. Wang, Z. You, D. Sun, J. Cui, W. Fan, Fabrication of Zn-MOF decorated BiVO4 photoanode for water splitting, Colloids Surf A Physicochem Eng Asp. 640 (2022) 128412. https://doi.org/10.1016/j.colsurfa.2022.128412.

[13] Y. Fan, G. Chen, D. Li, Y. Luo, N. Lock, A.P. Jensen, A. Mamakhel, J. Mi, S.B. Iversen, Q. Meng, B.B. Iversen, Highly selective deethylation of rhodamine B on TiO2 prepared in supercritical fluids, International Journal of Photoenergy. 2012 (2012) 1–7. https://doi.org/10.1155/2012/173865.

[14] S. Abbad, K. Guergouri, S. Gazaout, S. Djebabra, A. Zertal, R. Barille, M. Zaabat, Effect of silver doping on the photocatalytic activity of TiO2 nanopowders synthesized by the sol-gel route, J Environ Chem Eng. 8 (2020) 103718. https://doi.org/10.1016/j.jece.2020.103718.

[15] E. Valadez-Renteria, E. Barrera-Rendon, J. Oliva, V. Rodriguez-Gonzalez, Flexible CuS/TiO2 based composites made with recycled bags and polystyrene for the efficient removal of the 4-CP pesticide from drinking water, Sep Purif Technol. 270 (2021) 118821. https://doi.org/10.1016/j.seppur.2021.118821.

[16] H. Choi, E. Stathatos, D.D. Dionysiou, Photocatalytic TiO2 films and membranes for the development of efficient wastewater treatment and reuse systems, Desalination. 202 (2007) 199–206. https://doi.org/10.1016/j.desal.2005.12.055.

[17] S. BAKHTIARNIA, S. SHEIBANI, A. BILLARD, E. AUBRY, M. ARAB POUR YAZDI, Deposition of nanoporous BiVO4 thin-film photocatalyst by reactive magnetron sputtering: Effect of total pressure and substrate, Transactions of Nonferrous Metals Society of China. 32 (2022) 957–971. https://doi.org/10.1016/S1003-6326(22)65846-1.

[18] H. LI, J. ZHANG, G. HUANG, S. FU, C. MA, B. WANG, Q. HUANG, H. LIAO, Hydrothermal synthesis and enhanced photocatalytic activity of hierarchical flower-like Fe-

doped BiVO 4, Transactions of Nonferrous Metals Society of China. 27 (2017) 868–875. https://doi.org/10.1016/S1003-6326(17)60102-X.

[19] L. Chen, F.M. Toma, J.K. Cooper, A. Lyon, Y. Lin, I.D. Sharp, J.W. Ager, Mo-Doped BiVO 4 Photoanodes Synthesized by Reactive Sputtering, ChemSusChem. 8 (2015) 1066–1071. https://doi.org/10.1002/cssc.201402984.

[20] S. Fakhravar, M. Farhadian, S. Tangestaninejad, Excellent performance of a novel dual Z-scheme Cu2S/Ag2S/BiVO4 heterostructure in metronidazole degradation in batch and continuous systems: Immobilization of catalytic particles on α-Al2O3 fiber, Appl Surf Sci. 505 (2020) 144599. https://doi.org/10.1016/j.apsusc.2019.144599.

[21] S. Bakhtiarnia, S. Sheibani, E. Aubry, H. Sun, P. Briois, M. Arab Pour Yazdi, One-step preparation of Ag-incorporated BiVO4 thin films: plasmon-heterostructure effect in photocatalytic activity enhancement, Appl Surf Sci. 580 (2022) 152253. https://doi.org/10.1016/j.apsusc.2021.152253.

[22] R. Razi, S. Sheibani, Photocatalytic activity enhancement by composition control of mechano-thermally synthesized BiVO 4 -Cu 2 O nanocomposite, Ceram Int. (2021). https://doi.org/10.1016/j.ceramint.2021.07.151.

[23] Z. Xiang, Y. Wang, Z. Yang, D. Zhang, Heterojunctions of β-AgVO3/BiVO4 composites for enhanced visible-light-driven photocatalytic antibacterial activity, J Alloys Compd. 776 (2019) 266–275. https://doi.org/10.1016/j.jallcom.2018.10.287.

[24] P. Ju, Y. Wang, Y. Sun, D. Zhang, In-situ green topotactic synthesis of a novel Z-scheme Ag@AgVO3/BiVO4 heterostructure with highly enhanced visible-light photocatalytic

activity, J Colloid Interface Sci. 579 (2020) 431–447. https://doi.org/10.1016/j.jcis.2020.06.094.

[25] W. Zhao, J. Zhang, F. Zhu, F. Mu, L. Zhang, B. Dai, J. Xu, A. Zhu, C. Sun, D.Y.C. Leung, Study the photocatalytic mechanism of the novel Ag/p-Ag2O/n-BiVO4 plasmonic photocatalyst for the simultaneous removal of BPA and chromium(VI), Chemical Engineering Journal. 361 (2019) 1352–1362. https://doi.org/10.1016/j.cej.2018.12.181.

[26] R. Li, F. Zhang, D. Wang, J. Yang, M. Li, J. Zhu, X. Zhou, H. Han, C. Li, Spatial separation of photogenerated electrons and holes among {010} and {110} crystal facets of BiVO 4, Nat Commun. 4 (2013) 1–7. https://doi.org/10.1038/ncomms2401.

[27] L. Ge, Novel Pd/BiVO4 composite photocatalysts for efficient degradation of methyl orange under visible light irradiation, Mater Chem Phys. 107 (2008) 465–470. https://doi.org/10.1016/J.MATCHEMPHYS.2007.08.016.

[28] X. Chen, L. Li, T. Yi, W. Zhang, X. Zhang, L. Wang, Microwave assisted synthesis of sheet-like Cu/BiVO4 and its activities of various photocatalytic conditions, J Solid State Chem. 229 (2015) 141–149. https://doi.org/10.1016/J.JSSC.2015.05.026.

[29] C. Regmi, Y.K. Kshetri, R.P. Pandey, T.-H. Kim, G. Gyawali, S.W. Lee, Understanding the multifunctionality in Cu-doped BiVO4 semiconductor photocatalyst, Journal of Environmental Sciences. 75 (2019) 84–97. https://doi.org/10.1016/J.JES.2018.03.005.

[30] Y. Geng, P. Zhang, N. Li, Z. Sun, Synthesis of Co doped BiVO4 with enhanced visible-light photocatalytic activities, J Alloys Compd. 651 (2015) 744–748. https://doi.org/10.1016/J.JALLCOM.2015.08.123.

[31] D. Kong, J. Qi, D. Liu, X. Zhang, L. Pan, J. Zou, Ni-Doped BiVO4 with V4+ Species and Oxygen Vacancies for Efficient Photoelectrochemical Water Splitting, Transactions of Tianjin University. 25 (2019) 340–347. https://doi.org/10.1007/s12209-019-00202-1.

[32] M. Wang, C. Niu, J. Liu, Q. Wang, C. Yang, H. Zheng, Effective visible light-active nitrogen and samarium co-doped BiVO4 for the degradation of organic pollutants, J Alloys Compd. 648 (2015) 1109–1115. https://doi.org/10.1016/J.JALLCOM.2015.05.115.

[33] S.M. Thalluri, R.M. Rojas, O.D. Rivera, S. Hernández, N. Russo, S.E. Rodil, Chemically induced porosity on BiVO4 films produced by double magnetron sputtering to enhance the photo-electrochemical response, Physical Chemistry Chemical Physics. 17 (2015) 17821–17827. https://doi.org/10.1039/c5cp01561h.

[34] S. Ju, J. Jun, S. Son, J. Park, H. Lim, W. Kim, D. Chae, H. Lee, Structured BiVO4Photoanode Fabricated via Sputtering for Large Areas and Enhanced Photoelectrochemical Performance, ACS Sustain Chem Eng. (2020). https://doi.org/10.1021/acssuschemeng.0c05225.

[35] E. Aubry, P. Miska, L. Gigleux, A. Mézin, V. Demange, A. Billard, Microstructural and photocatalytic properties distribution of TiO2 coatings reactively sputtered as a function of the substrate position relatively to the Ti target, Surf Coat Technol. 202 (2008) 4980–4985. https://doi.org/10.1016/j.surfcoat.2008.04.097.

[36] S. Sarkar, N.S. Das, K.K. Chattopadhyay, Optical constants, dispersion energy parameters and dielectric properties of ultra-smooth nanocrystalline BiVO4 thin films prepared by rf-magnetron sputtering, Solid State Sci. 33 (2014) 58–66. https://doi.org/10.1016/j.solidstatesciences.2014.04.008.

[37] A. Walsh, Y. Yan, M.N. Huda, M.M. Al-Jassim, S.-H. Wei, Band Edge Electronic Structure of BiVO 4 : Elucidating the Role of the Bi s and V d Orbitals, Chemistry of Materials. 21 (2009) 547–551. https://doi.org/10.1021/cm802894z.

[38] J. Guo, X. Liao, M.-H. Lee, G. Hyett, C.-C. Huang, D.W. Hewak, S. Mailis, W. Zhou, Z. Jiang, Experimental and DFT insights of the Zn-doping effects on the visible-light photocatalytic water splitting and dye decomposition over Zn-doped BiOBr photocatalysts, Appl Catal B. 243 (2019) 502–512. https://doi.org/10.1016/J.APCATB.2018.09.089.

[39] K.V. Kumar, K. Porkodi, F. Rocha, Langmuir-Hinshelwood kinetics - A theoretical study, Catal Commun. 9 (2008) 82–84. https://doi.org/10.1016/j.catcom.2007.05.019.

[40] J. Cao, X. Wang, A. Tang, X. Wang, Y. Wang, W. Wu, Sol–gel synthesis and electrochemical properties of CuV2O6 cathode material, J Alloys Compd. 479 (2009) 875–878. https://doi.org/10.1016/j.jallcom.2009.01.095.

[41] C. Regmi, Y.K. Kshetri, R.P. Pandey, T.-H. Kim, G. Gyawali, S.W. Lee, Understanding the multifunctionality in Cu-doped BiVO4 semiconductor photocatalyst, Journal of Environmental Sciences. 75 (2019) 84–97. https://doi.org/10.1016/j.jes.2018.03.005.

[42] W.J. Jo, H.J. Kang, K.-J. Kong, Y.S. Lee, H. Park, Y. Lee, T. Buonassisi, K.K. Gleason, J.S. Lee, Phase transition-induced band edge engineering of BiVO 4 to split pure water under visible light, Proceedings of the National Academy of Sciences. 112 (2015) 13774–13778. https://doi.org/10.1073/pnas.1509674112.

[43] P. Yang, L. Li, S. Yu, H. Zheng, W. Peng, The annealing temperature and films thickness effect on the surface morphology, preferential orientation and dielectric property of NiO films, Appl Surf Sci. 493 (2019) 396–403. https://doi.org/10.1016/j.apsusc.2019.06.223.

[44] M.C. Biesinger, L.W.M. Lau, A.R. Gerson, R.St.C. Smart, Resolving surface chemical states in XPS analysis of first row transition metals, oxides and hydroxides: Sc, Ti, V, Cu and Zn, Appl Surf Sci. 257 (2010) 887–898. https://doi.org/10.1016/j.apsusc.2010.07.086.

[45] S. Behjati, S. Sheibani, J. Herritsch, J.M. Gottfried, Photodegradation of dyes in batch and continuous reactors by Cu2O-CuO nano-photocatalyst on Cu foils prepared by chemical-thermal oxidation, Mater Res Bull. 130 (2020) 110920. https://doi.org/10.1016/j.materresbull.2020.110920.

[46] M.C. Biesinger, Advanced analysis of copper X-ray photoelectron spectra, Surface and Interface Analysis. 49 (2017) 1325–1334. https://doi.org/10.1002/sia.6239.

[47] S.K. Sengar, B.R. Mehta, Govind, Size and alloying induced shift in core and valence bands of Pd-Ag and Pd-Cu nanoparticles, J Appl Phys. 115 (2014) 124301. https://doi.org/10.1063/1.4869437.

[48] M. Wang, P. Guo, T. Chai, Y. Xie, J. Han, M. You, Y. Wang, T. Zhu, Effects of Cu dopants on the structures and photocatalytic performance of cocoon-like Cu-BiVO4 prepared via ethylene glycol solvothermal method, J Alloys Compd. 691 (2017) 8–14. https://doi.org/10.1016/J.JALLCOM.2016.08.198.

[49] G. Silversmit, D. Depla, H. Poelman, G.B. Marin, R. de Gryse, Determination of the V2p XPS binding energies for different vanadium oxidation states (V5+ to V0+), J Electron Spectros Relat Phenomena. 135 (2004) 167–175. https://doi.org/10.1016/j.elspec.2004.03.004.

[50] J. Landoulsi, M.J. Genet, S. Fleith, Y. Touré, I. Liascukiene, C. Méthivier, P.G. Rouxhet, Organic adlayer on inorganic materials: XPS analysis selectivity to cope with adventitious

contamination, Appl Surf Sci. 383 (2016) 71–83. https://doi.org/10.1016/j.apsusc.2016.04.147.

[51] S. Xue, H. He, Z. Wu, C. Yu, Q. Fan, G. Peng, K. Yang, An interesting Eu,F-codoped BiVO4 microsphere with enhanced photocatalytic performance, J Alloys Compd. 694 (2017) 989–997. https://doi.org/10.1016/J.JALLCOM.2016.10.146.

[52] I. Khan, S. Ali, M. Mansha, A. Qurashi, Sonochemical assisted hydrothermal synthesis of pseudo-flower shaped Bismuth vanadate (BiVO4) and their solar-driven water splitting application, Ultrason Sonochem. 36 (2017) 386–392. https://doi.org/10.1016/J.ULTSONCH.2016.12.014.

[53] Z. Ding, Y. Fu, Z. Xie, Z. Li, A polymeric complex method to nanocrystalline BiCu2VO6 with visible light photocatalytic activity, Mater Lett. 65 (2011) 460–463. https://doi.org/10.1016/j.matlet.2010.10.063.

[54] B. Pattengale, J. Huang, The effect of Mo doping on the charge separation dynamics and photocurrent performance of BiVO4 photoanodes, Physical Chemistry Chemical Physics. 18 (2016) 32820–32825. https://doi.org/10.1039/c6cp06407h.

[55] J.F. Deng, H. Li, W. Wang, Progress in design of new amorphous alloy catalysts, Catal Today. 51 (1999) 113–125. https://doi.org/10.1016/S0920-5861(99)00013-9.

[56] S. Guo, S. Han, H. Mao, S. Dong, C. Wu, L. Jia, B. Chi, J. Pu, J. Li, Structurally controlled ZnO/TiO2 heterostructures as efficient photocatalysts for hydrogen generation from water without noble metals: The role of microporous amorphous/crystalline composite structure, J Power Sources. 245 (2014) 979–985. https://doi.org/10.1016/j.jpowsour.2013.07.044.

[57] C. Regmi, Y.K. Kshetri, T.-H. Kim, R.P. Pandey, S.K. Ray, S.W. Lee, Fabrication of Ni-doped BiVO4 semiconductors with enhanced visible-light photocatalytic performances for wastewater treatment, Appl Surf Sci. 413 (2017) 253–265. https://doi.org/10.1016/J.APSUSC.2017.04.056.

[58] L. Zhang, B. Han, P. Cheng, Y.H. Hu, In-situ FTIR-DRS investigation on shallow trap state of Cu-doped TiO2 photocatalyst, Catal Today. 341 (2020) 21–25. https://doi.org/10.1016/j.cattod.2018.06.049.

[59] S. Park, W. Kim, Y. Kim, Photodegradation of organic dyes via competitive direct reduction/indirect oxidation on InSnS2 under visible light, Korean Journal of Chemical Engineering. 34 (2017) 1500–1503. https://doi.org/10.1007/s11814-017-0034-0.

[60] Y. Nosaka, A.Y. Nosaka, Generation and Detection of Reactive Oxygen Species in Photocatalysis, Chem Rev. 117 (2017) 11302–11336. https://doi.org/10.1021/acs.chemrev.7b00161.

[61] Y. Kanigaridou, A. Petala, Z. Frontistis, M. Antonopoulou, M. Solakidou, I. Konstantinou, Y. Deligiannakis, D. Mantzavinos, D.I. Kondarides, Solar photocatalytic degradation of bisphenol A with CuO x /BiVO 4 : Insights into the unexpectedly favorable effect of bicarbonates, Chemical Engineering Journal. 318 (2017) 39–49. https://doi.org/10.1016/j.cej.2016.04.145.

[62] S. Obregón, G. Colón, On the different photocatalytic performance of BiVO4 catalysts for Methylene Blue and Rhodamine B degradation, J Mol Catal A Chem. 376 (2013) 40–47. https://doi.org/10.1016/j.molcata.2013.04.012.

[63] A. Lebedev, F. Anariba, X. Li, P. Wu, Rational design of visible-light-sensitive Ag-BiVO4 oxides by matching redox potentials of catalyst, dyes, and reactive oxygen species towards more efficient photocatalytic degradation, J Environ Chem Eng. 8 (2020). https://doi.org/10.1016/j.jece.2020.103748.

[64] K. Krumova, G. Cosa, Chapter 1. Overview of Reactive Oxygen Species, in: 2016: pp. 1–21. https://doi.org/10.1039/9781782622208-00001.

[65] E. Aguilera-Ruiz, U.M. García-Pérez, M. de la Garza-Galván, P. Zambrano-Robledo, B. Bermúdez-Reyes, J. Peral, Efficiency of Cu2O/BiVO4 particles prepared with a new soft procedure on the degradation of dyes under visible-light irradiation, Appl Surf Sci. 328 (2015) 361–367. https://doi.org/10.1016/J.APSUSC.2014.12.059.

[66] B. Zhou, J. Qu, X. Zhao, H. Liu, Fabrication and photoelectrocatalytic properties of nanocrystalline monoclinic BiVO4 thin-film electrode, Journal of Environmental Sciences. 23 (2011) 151–159. https://doi.org/10.1016/S1001-0742(10)60387-7.

[67] Y. Zhang, Z. Yi, G. Wu, Q. Shen, Novel Y doped BiVO4 thin film electrodes for enhanced photoelectric and photocatalytic performance, J Photochem Photobiol A Chem. 327 (2016) 25–32. https://doi.org/10.1016/j.jphotochem.2016.05.004.

[68] B. Zhou, X. Zhao, H. Liu, J. Qu, C.P. Huang, Synthesis of visible-light sensitive M–BiVO4 (M = Ag, Co, and Ni) for the photocatalytic degradation of organic pollutants, Sep Purif Technol. 77 (2011) 275–282. https://doi.org/10.1016/J.SEPPUR.2010.12.017.